

ARTICLE OPEN



Inorganic–organic hybrid quantum dots for AOP-mediated photodegradation of ofloxacin and para-nitrophenol in diverse water matrices

Soumya Ranjan Mishra¹, Vishal Gadore¹ and Md. Ahmaruzzaman¹✉

Due to concerns about the accessibility of clean water and the quality of treated wastewater, developing a suitable solution to enhance the water quality is critical. Thus, the current study focused on the synthesis of cadmium-doped CdIn₂S₄ incorporated in chitosan, forming Cd/CdIn₂S₄@Ch quantum dots using a solvothermal technique for the efficient photodegradation of hazardous pollutants like ofloxacin and para-nitrophenol through H₂O₂-mediated AOP. Cd/CdIn₂S₄@Ch quantum dots were characterized by several advanced methods, including XRD, PL, UV-DRS, FTIR, SEM, HR-TEM, XPS, DSC, TGA, EDX, and Elemental mapping analysis. The influence of varying reaction parameters, such as the effect of organic compounds, inorganic ions, and water matrices, was also investigated. The prepared composite showed outstanding photodegradation efficiency of 85.51 ± 1.35% and 96.70 ± 1.31%, with a rate constant of 0.02334 and 0.15134 min⁻¹, which is about 1.24 and 2.07 times higher than pristine CdIn₂S₄ for ofloxacin and para-nitrophenol, respectively. The COD values were reduced to 80.67 ± 1.67% for ofloxacin and 88.36 ± 1.43% for para-nitrophenol, whereas the TOC values reduced to 73.49% and 86.34%, respectively, from their initial values. The improved performance is ascribed to the encapsulation of CdIn₂S₄ by chitosan, leading to the self-doping of cadmium into the photocatalyst, as the incorporated cadmium doping site can generate a local electron accumulation point, improving the charge separation efficacy and surface charge mitigation capability of chitosan nanosheets even further. The scavenger experiments showed that hydroxyl and superoxide radicals played a significant part in the photodegradation of contaminants. Additionally, the quantum dots showed excellent constancy and were recyclable up to six times, suggesting exceptional stability and reusability of the manufactured photocatalyst. The fabricated Cd/CdIn₂S₄@Ch quantum dots could be an excellent photocatalyst for removing organic pollutants from wastewater in the near future.

npj Clean Water (2023)6:78; <https://doi.org/10.1038/s41545-023-00291-5>

INTRODUCTION

Numerous organic and inorganic chemicals, such as dyes, pharmaceuticals, pesticides and personal care products, have been regularly released into the environment without any proper treatment in recent years as human civilization has grown¹. The lack of drinking water poses a potential global threat to humans. Above this, most of these contaminants are chemically stable and resilient to biological degradation^{2,3}. Ofloxacin (OFL) is a pharmaceutical compound associated with the fluoroquinolone family and is widely used as an antimicrobial agent. The human body cannot metabolize fluoroquinolone completely, and about 20–80% of it is excreted in biologically active forms⁴. Bacteria may experience gene changes due to exposure to antimicrobial residues found in environmental matrices, creating bacteria that are resistant to the drug. Drug-resistant microorganisms force the employment of more potent medications to treat diseases. Moreover, the antibiotics could not be entirely eliminated in the wastewater treatment plants, causing bioaccumulation and environmental toxicity⁵. OFL residues in aquatic habitats can infiltrate human bodies through the food chain or even drinking water when pharmaceutical effluent and animal manure are not adequately treated. Due to its enduring resistance to biodegradation, it persisted in the environment for a long time. As a result, the removal of OFL is limited by common methods. Therefore, it is crucial to employ treatment techniques to eliminate these chemicals' remaining antibacterial activity.

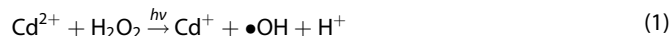
Moreover, para-nitrophenol (PNP) is a toxic carbon-based organic compound widely used to manufacture pesticides, drugs, dyes, etc. In low concentrations, PNP causes skin irritation, headache, and nausea⁶. A higher concentration of PNP is toxic to animals and is the cause of methemoglobinemia in humans. Issues such as breathing difficulties, collapse, and even death might result from more elevated amounts. PNP causes fever, weakness, dizziness, and stomach trouble at lower concentrations. Prolonged or high exposures may impact the nervous system. Thus, these toxic contaminants must be removed from the water bodies efficiently and effectively⁷. Although various conventional water treatment methods like liquid phase adsorption, physico-chemical treatment, and biological treatments were used to purify water, they have several limitations: low efficiency, low reusability, uneconomical operational cost, and may cause secondary pollution⁸.

Furthermore, most of the research focuses on the reduction of para-nitrophenol to para-aminophenol utilizing hazardous reducing agents that further pollute the environment. Additionally, these methods have several disadvantages since it requires extreme temperature and pressures⁹. Therefore, researchers are incessantly developing approaches to eliminate pollutants from water with greater efficiency, low cost, and without generating any by-products.

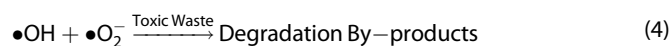
The advanced oxidation process (AOP) has arisen as an effective method for mineralizing organic pollutants and has grown much

¹Department of Chemistry, National Institute of Technology, Silchar, Assam 788010, India. ✉email: mda2002@gmail.com

attention due to its simplicity and low-cost¹⁰. Recently, AOPs involving heterogeneous photocatalysts, the Fenton process, the Electro-Fenton process, and the Photo-Fenton process have been utilized to generate reactive radicals, which then degrade organic contaminants from wastewater (Eq. 1)¹¹:



In the general AOPs, to create photoinduced electron–hole pairs, the semiconducting photocatalyst is radiated with photon energy that is equivalent to or higher than its bandgap energy in this process¹². These photoinduced electrons and holes react with water and adsorbed oxygen to initiate a series of reactions producing reactive oxygen species (ROSS), which later degrade complex toxic waste into more minor by-products according to the following equations (Eqs. 2–4)¹³:



For the photocatalyst to have increased photocatalytic activity, photoinduced electrons (e^-) and holes (h^+) must be separated. The charge carriers can be separated by transferring charges, which requires separating e^- and h^+ , or by sorption on the semiconductor surface. The breakdown of dangerous organic pollutants into less damaging substances like CO_2 and H_2O is made possible by the coordinated action of these radicals. AOP is promoted as an efficient wastewater remediation technology owing to its improved degrading efficiency, low cost, and comfortable operating conditions. The Photo-Fenton-Like method is one type of AOP frequently used to remove toxic contaminants¹⁴. H_2O_2 is employed in a Photo-Fenton-like process to create ROSS, which continue to degrade the organic pollutants in water.

Given their greater surface area, vigor catalytic activity, and morphology-dependent physicochemical characteristics, nanomaterials have received more attention as potential materials for wastewater treatment¹⁵. Due to cost-efficiency, non-toxicity, and high stability, titanium dioxide has been extensively explored as a semiconductor photocatalyst for various photocatalytic applications¹⁶. However, due to a higher bandgap and higher electron–hole recombination adversely limit its practical applications. Hence, developing an enhanced visible light-active photocatalyst is necessary to utilize solar irradiation properly. Additionally, several methods like doping, heterojunction formation, or using a support material for photocatalyst stabilization could slow down the charge recombination rate, further enhancing the stability and efficiency of the prepared photocatalyst^{11,17,18}.

Recent years have seen much interest in ternary chalcogenides due to their distinct optoelectronic and catalytic properties. For instance, ZnIn_2S_4 , AgIn_5S_8 , CdIn_2S_4 , etc., have been utilized for various photocatalytic applications, as the covalent bonding is more distinct in sulfospinel than the oxyspinels¹⁹. Among these, CdIn_2S_4 showed an ideal bandgap of around 2.18 eV, making it an appropriate catalyst under visible light radiation²⁰. He et al.²¹ produced CdIn_2S_4 via the hydrothermal technique for electrocatalytic application. Liang et al.²² used solvothermal synthesized CdIn_2S_4 as a catalyst for organic synthesis. CdIn_2S_4 synthesized via a hydrothermal method was applied to photodegrade dyes from wastewater²³. CdIn_2S_4 is a ternary chalcogenide with a chemically stable spinel cubic nanostructure and acts as an effective photocatalyst. However, pristine CdIn_2S_4 suffers from a faster charge recombination rate limitation, thereby lowering its photocatalytic efficiency. Therefore, supporting and doping CdIn_2S_4 could increase its efficiency by suppressing the charge

recombination rate. For example, CdIn_2S_4 supported on UiO-66 showed enhanced degradation of triclosan from water²⁴. Researchers have also synthesized metal-doped CdIn_2S_4 supported on the $\text{g-C}_3\text{N}_4$ surface for photodegradation of methyl orange²⁵. Chitosan (Ch) is an organic biopolymer known for its adsorption capacity²⁶. A linear polysaccharide chain comprised of irregularly linked D-glucosamine and N-acetyl-D-glucosamine units makes up the natural biopolymer chitosan structure. Chitosan is a desirable material to support ternary metal sulfide nanoparticles due to its non-toxic, biocompatible, and biodegradable characteristics. Because of its amine ($-\text{NH}_2$) and hydroxyl (OH) groups, chitosan is a superior adsorbent for a variety of organic pollutants²⁷.

Herein, a $\text{Cd}/\text{CdIn}_2\text{S}_4/\text{Ch}$ quantum dot has been synthesized via a solvothermal method at slightly higher temperatures (160 °C). The in situ interstitial doping of cadmium onto CdIn_2S_4 self-assembled on chitosan biopolymer led to the formation of a hybrid inorganic–organic nanostructure. The fabricated quantum dots were characterized using XRD, PL, UV-DRS, FTIR, SEM, HR-TEM, XPS, DSC, TGA, EDX, and Elemental mapping analysis. The catalytic photoactivity of the manufactured composite has been examined by investigating the degradation of ofloxacin (OFL) and para-nitrophenol (PNP) under visible light irradiation in the presence of hydrogen peroxide, which are potential emerging pollutants commonly found in water. The composite exhibited outstanding photodegradation efficiency of $85.51 \pm 1.35\%$ and $96.70 \pm 1.31\%$ for ofloxacin and para-nitrophenol, respectively, with a rate constant of 0.02334 and 0.15134 min^{-1} , which is higher than most of the previously reported studies. In addition to these, the photodegradation efficiency was also investigated in the existence of various organic compounds, cations, anions, waters, and salinity levels to confirm the use of the photocatalyst in real-life applications. Furthermore, the TOC, COD, quantum yield, and figure of merits (FoM) values were also measured for various systems to investigate the true potential of the fabricated material. The mechanism of photodegradation of ofloxacin and para-nitrophenol, along with the intermediate transformation products, is also illustrated based on the experimental findings.

RESULTS AND DISCUSSION

Crystal structure analysis

Figure 1a illustrates the results of an XRD examination conducted to examine the orientation and crystal structure of the synthesized CdIn_2S_4 and $\text{Cd}/\text{CdIn}_2\text{S}_4/\text{Ch}$, respectively. The synthesized pristine CdIn_2S_4 showed 2θ values of 14.14° , 23.20° , 27.25° , 28.52° , 33.02° , 40.76° , 43.33° , 47.55° , 49.71° , 53.41° , 55.56° , 59.07° , 64.21° , 66.25° , 69.31° , 76.00° , and 78.95° , which were corresponding to (1 1 1), (2 2 0), (3 1 1), (2 2 2), (4 0 0), (4 2 2), (5 1 1), (4 4 0), (5 3 1), (6 2 0), (5 3 3), (4 4 4), (6 4 2), (7 3 1), (8 0 0), (6 6 0), and (8 4 0) planes, respectively²⁸. These planes were attributed to the cubic system of CdIn_2S_4 , having a face-centered lattice with a lattice parameter of $\alpha = 10.84 \text{ \AA}$, as all the representing peaks were following the Joint Committee's database on Powder Diffraction Standards (JCPDS card no: 27-0060). However, in the prepared $\text{Cd}/\text{CdIn}_2\text{S}_4/\text{Ch}$ quantum dots, a red shift in the XRD peaks was detected due to the introduction of dopant (Cd) to the host (CdIn_2S_4)²⁹. The 2θ values of 14.41° , 23.45° , 27.42° , 28.69° , 44.22° , and 47.81° were designated to the (1 1 1), (2 2 0), (3 1 1), (2 2 2), (5 1 1), and (4 4 0) planes, respectively. This peak shift was attributed to a change in the size of the host and the strong linkage between the dopant and the host. In addition to that, as the CdIn_2S_4 was developed on the surface of the Chitosan biopolymer, a rearrangement of lattice structures occurred, leading to competitive stress, which resulted in the right shift of XRD peaks³⁰. This rearrangement of the lattice structure led to the incorporation of Cadmium into the photocatalyst. The peak at 38.32° was attributed to the (1 0 1) plane of

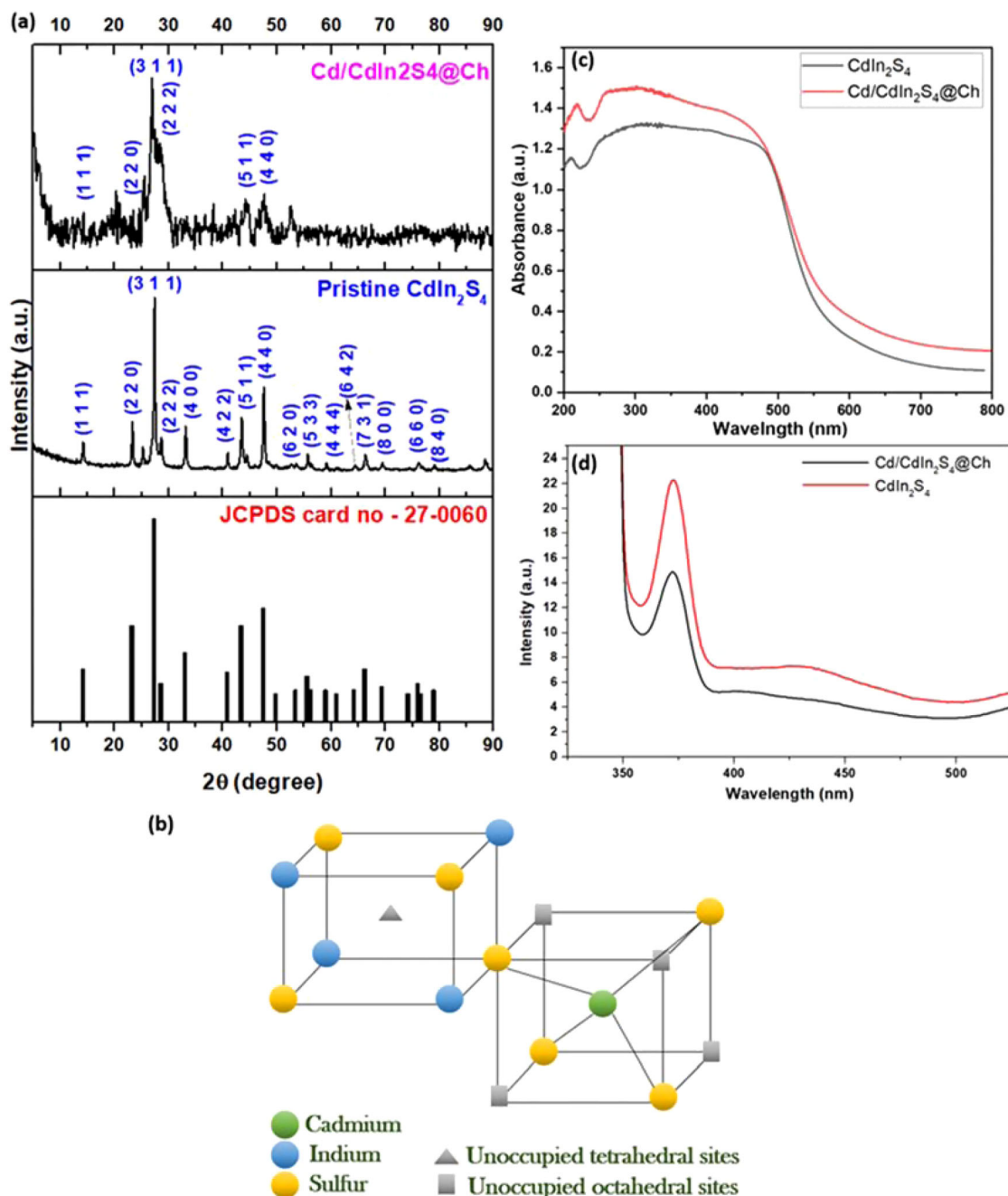


Fig. 1 Structural and optical analysis of fabricated nanocomposites. **a** XRD analysis of pristine CdIn₂S₄ and Cd/CdIn₂S₄@Ch. **b** Lattice structure of CdIn₂S₄. **c** UV-DRS spectra of pristine CdIn₂S₄ and Cd/CdIn₂S₄@Ch. **d** PL spectra analysis.

the cadmium metal, as confirmed by the JCPDS card no: 85-1328. The peak at 20.21°, corresponding to the plane (2 2 0), confirmed the presence of chitosan in the fabricated photocatalyst³¹. Cadmium was incorporated into the created photocatalyst because Cd's ionic radius is too small compared to CdIn₂S₄, resulting in a shift toward a greater angle, causing the lattice parameter to decrease. After the photocatalyst formation, the intensity of a few planes altered. Some peaks changed in intensity while others decreased due to the doped atom's different electron density from the atoms around it³². The average crystalline size was 15.162 nm for pristine CdIn₂S₄ and 1.572 nm for Cd/CdIn₂S₄@Ch quantum dots and was calculated using the Scherrer formula, as shown in Eq. (5). The decrease in crystallite size

confirmed the lattice strain and right shift of the XRD peaks. In addition, the pristine CdIn₂S₄ showed a very high crystallinity of 84.81%, whereas, for the nanocomposite, the crystallinity decreased to 49.02%. This phenomenon occurred due to the addition of chitosan, which increased the amorphous characteristics, resulting in a lower signal-to-noise ratio. In Eq. (5), 'D' is the size of crystallite (nm), k is the shape factor (0.89), λ is the CuKα1 radiation wavelength (1.54060 Å), β is the full width at half maximum (FWHM) for a given peak, and θ is the Bragg's angle of diffraction.'

$$D = \frac{k\lambda}{\beta \cos\theta} \quad (5)$$

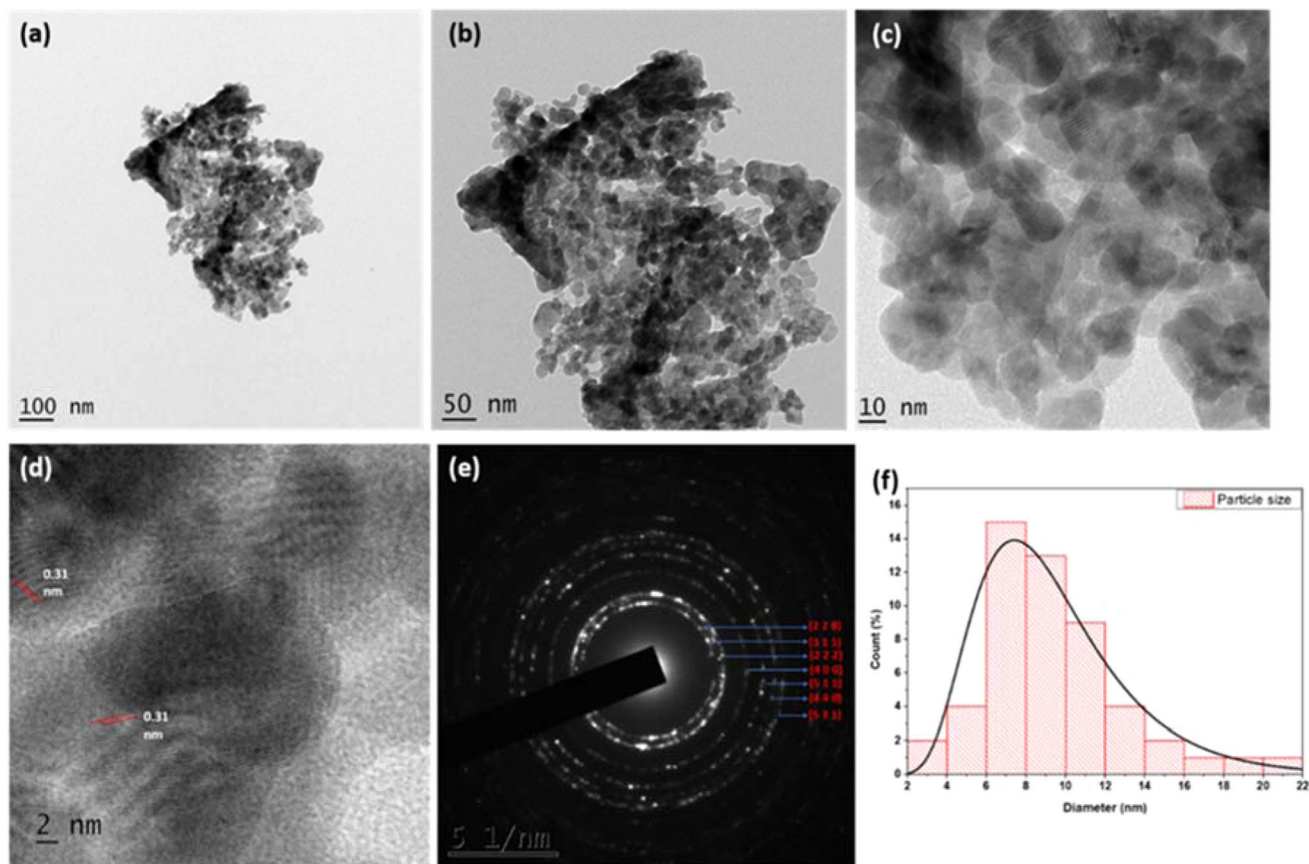


Fig. 2 TEM analysis of synthesized Cd/CdIn₂S₄@Ch quantum dots. **a, b** TEM images. **c, d** HR-TEM Images. **e** SAED pattern. **f** Particle size distribution curve.

The fabricated CdIn₂S₄ follows an A²⁺B₂³⁺X₄²⁻ spinel structure, where the anions are arranged in a cubic closed-packed lattice, and the cations in octahedral and tetrahedral sites (Fig. 1b). With eight tetrahedral and four octahedral sites per formula unit, cubic close-packed oxides make up the majority of spinel structures. There are fewer tetrahedral spaces than octahedral spaces. A ions occupy one-eighth of the tetrahedral holes, whereas B ions fill half of the octahedral holes³³. In this case, the cadmium ions are present in the tetrahedral sites, while the indium ions are in the octahedral sites. However, after encapsulation of chitosan, the rearrangement due to lattice strain led to the incorporation of cadmium in the unoccupied tetrahedral or the octahedral sites, resulting in interstitial doping. The decrease in lattice parameters confirms the formation of Cd/CdIn₂S₄@Ch quantum dots.

Optical properties

The absorbance spectra of pristine CdIn₂S₄ and Cd/CdIn₂S₄@Ch quantum dots were recorded in the 200 to 800 nm range for insight into their optical properties. The UV–vis diffuse reflectance spectra (DRS) of pure CdIn₂S₄ and Cd/CdIn₂S₄@Ch are shown in Fig. 1c. CdIn₂S₄ displays a broad absorption curve with an absorption edge at around 600 nm, while the absorption edge was shifted to a higher wavelength at around 650 nm for Cd/CdIn₂S₄@Ch, suggesting the formation of heterojunction and doping of Cd into the composite. The red shift in the absorption edge indicates a possible transition of e⁻ from the VB to the CB and delayed recombination. Tauc's plot was used to calculate the indirect bandgap of the prepared samples. Pure CdIn₂S₄ has a bandgap of 2.1 eV, which is slightly increased to 2.2 eV for the Cd/CdIn₂S₄@Ch, indicating a smaller particle size for the final

nanocomposite, as illustrated in Supplementary Fig. 1a. Moreover, the bandgap values are in good agreement with the previously reported bandgap (2.1–2.5 eV)³⁴.

Photoluminescence (PL) spectroscopy was used further to evaluate the optical properties of the prepared photocatalysts. PL is a reliable technique to study the recombination of photogenerated electron–hole pairs in the pristine CdIn₂S₄ and the Cd/CdIn₂S₄@Ch nanocomposite. The samples were excited at a wavelength of 330 nm, and the corresponding emission spectra were obtained, as illustrated in Fig. 1d. The composite's spectra are similar to pure CdIn₂S₄ but with lower intensity. A decreased intensity was credited to enhanced charge separation and a slower recombination rate³⁵. A sharp peak at a wavelength of around 373 nm could have originated due to the excitation of electrons from the VB to the CB in CdIn₂S₄³⁶. This inference suggested that the prepared nanocomposite has greater charge separation and photocatalytic activity than pure CdIn₂S₄.

TEM analysis

Transmission electron microscopy (TEM) was conducted to evaluate further the shape and size of the fabricated Cd/CdIn₂S₄@Ch quantum dots. Both TEM (Fig. 2a, b) and HR-TEM images (Fig. 2c, d) revealed irregularly shaped particles with definite grain boundaries. Figure 2d showed the interplanar spacing of 0.31 nm, which corresponded to the plane (2 2 2) and was in accordance with the XRD data as its peak exhibited the highest intensity. The polycrystalline character of the developed Cd/CdIn₂S₄@Ch quantum dots was demonstrated by the selected area electron diffraction (SAED) pattern (Fig. 2e). Although the results acquired were connected with the extremely strong peak in XRD, they were not entirely compatible with the JCPDS data

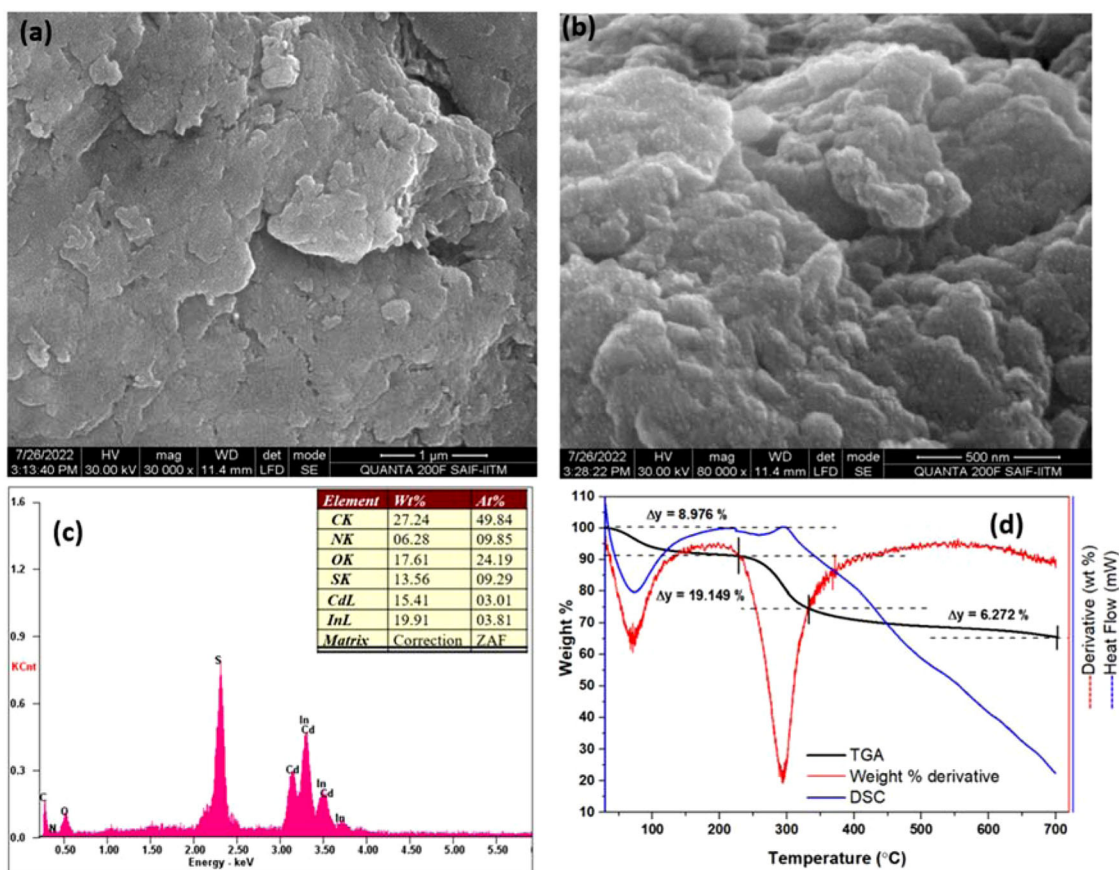


Fig. 3 SEM/EDX and TGA/DSC analysis of Cd/CdIn₂S₄@Ch quantum dots. **a, b** SEM images. **c** EDX analysis. **d** TGA/DSC analysis.

d-spacing values. This observation was attributed to the redshift of the XRD spectra, as the d-spacing and 2θ values are closely related to each other via Bragg law, implying that a rise in 2θ values resulted in a decrease in d-spacing values. Moreover, some rings in the SAED image were diffused, which confirmed the relatively small crystal size. In addition, the bright concentric rings were due to the high crystallinity of the fabricated photocatalyst³⁷. Moreover, the SAED pattern agreed with the *hkl* planes d-spacing obtained from the XRD data investigation. A quantitative analysis of a histogram fitted with the Lorentzian function revealed that the average size of particles from TEM images was 7.35 nm (Fig. 2f). The average particle size and the crystalline particle size were correlated because a particle's crystalline size might differ by up to 20 nm from its average particle size³⁸.

SEM and EDX analysis

The surface topographic anatomy of the manufactured Cd/CdIn₂S₄@Ch quantum dots, comprising the microporous and mesoporous geomorphology, was established using scanning electron microscopy (SEM), exhibiting sheet-like morphology (Fig. 3a, b). This demonstrated that CdIn₂S₄ was encapsulated by chitosan after self-assembling on its surface. As illustrated in Fig. 3b, the photocatalysts were uneven in shape, and the Cd/CdIn₂S₄@Ch surface was relatively rough. Furthermore, certain surface fractures that were discovered were due to nanocomposite generation. We concluded that CdIn₂S₄ and Chitosan biopolymer grafting caused the nanocomposite surface to become rough and flake-like³⁹. The uneven and porous shape boosted contaminant molecule adsorption, increasing the photocatalytic activity⁴⁰. The distribution of elements in the synthesized Cd/CdIn₂S₄@Ch quantum dots was evaluated further by EDX and depicted in Fig. 3c. The elements identified in the composite

structure of the prepared photocatalyst were carbon, oxygen, nitrogen, sulfur, cadmium, and indium, with weight percentages of 27.24, 17.61, 6.28, 13.56, and 15.41, respectively, without any other elemental impurities. The atomic percentage suggested that the cadmium, indium, and sulfur were present in a ratio close to 1:2:4, and the higher extra atomic content of cadmium inferred the presence of it as a dopant. The persistence of chitosan in the hybrid composite matrix is responsible for the high atomic proportions of carbon, oxygen, and nitrogen in the photocatalyst⁴⁰.

TGA/DSC analysis

The thermal decomposition curves (DSC/TGA) of Cd/CdIn₂S₄@Ch quantum dots are shown in Fig. 3d. The weight fluctuation of the specimen was plotted using TGA data, while DSC identified whether the reaction was exothermic or endothermic. Weight derivative (temp) provided the details on the rate at which weight changes relative to temperature⁴¹. The TGA plot shows that the fabricated Cd/CdIn₂S₄@Ch quantum dots underwent three degradation stages. An initial weight loss of 8.976% was detected, which was attributed to the endothermic evaporation of water. The second degradation stage at around 220 °C resulted in a slightly higher weight loss of 19.149%, which may be due to the disruption of physical interaction between the organic and inorganic moieties, while the third degradation stage starting at around 340 °C was due to the disintegration of chitosan biopolymer, which led to a weight loss of about 6.272%. Even after increasing the temperature to 700 °C at a rate of 10 °C/min, the synthesized material only showed a weight loss of 35%, which exhibited its stability and sustainability even in adverse conditions. At 75 °C and 320 °C, the specimen lost weight, caused by the evaporation of water and organic by-products. The evaporation of

adsorbed water and water ligands can be attributed to an endothermic peak with a temperature of around 75 °C. When heated from room temperature to 200 °C, the chitosan-based nanocomposite showed no endothermic transition, indicating no crystalline or other phase change⁴². The sample's oxidative decay was responsible for the strong exothermic peak with a peak temperature of 320 °C due to the self-assembling nanocomposite's structural integrity that was generally impacted by the chelation process involving the NH group of chitosan. Moreover, the weight derivative curve followed the DSC curve, further confirming the sudden weight change during the sample's endothermic and exothermic degradation at temperatures of 75 and 320 °C, respectively.

Chemical environment analysis

The chemical environment of the surface and oxidation states of the components in the Cd/CdIn₂S₄@Ch quantum dots were investigated using the XPS technique. As shown in Fig. 4a, the survey spectrum illustrated the presence of Cd, In, S, C, N, and O elements in the photocatalyst. Moreover, all elements' atomic concentration has been calculated from the base peak area, as summarized in Supplementary Table 1. A doublet at 404.97 eV and 411.75 eV in the Cd 3d spectral region is related to the Cd 3d_{5/2} and Cd 3d_{3/2} microstates of Cd²⁺ species in sulfide environments (Fig. 4b)⁴³. In the de-convoluted short scan In 3d spectrum, the two peaks at 444.62 eV and 452.18 eV were allotted to 3d_{5/2} and 3d_{3/2} states of In³⁺ ions in coordination with sulfide ions (Fig. 4c)⁴⁴. The presence of doped Cd⁰ can be proved in Fig. 4d, where the Cd 3d_{5/2} was further de-convoluted to obtain peaks at 405.41 eV and 404.78 eV that were assigned to Cd⁺² and Cd⁰ ion, respectively⁴⁵. It was also observed that the peaks of Cd 3d and In 3d spectrum showed a redshift, i.e., a decrease in the binding energy than the normal values²⁴. This inference may be attributed to the electronegativity of the doping element (Cd = 1.69 eV), which is lower than the base element (CdIn₂S₄ = 4.78 eV) as the electron density around it increases, and the binding energy decreases. The peaks exhibited for S 2p, as illustrated in Fig. 4e, are indexed at 162.34 eV and 161.33 eV, attributed to 2p_{1/2} and 2p_{3/2} of S, which corresponds to sulfide anions and terminal polysulfide⁴⁶. It demonstrates that sulfur moiety instantly links to In³⁺ and Cd²⁺ and then clings to the chitosan moiety. From the short scan spectra of sulfur and cadmium, the existence of Cd/CdIn₂S₄ can also be inferred. In the XPS spectrum for carbon C 1s, as illustrated by Fig. 4f, three distinct peaks were observed at 284.79 eV, 286.23 eV, and 287.85 eV; these show the existence of C–C, C–H; C–O–C, C–N and C–OH; and C=O and O–C=O bond present in the chitosan matrix correspondingly⁴⁷. In the de-convoluted short scan XPS spectrum of oxygen O 1s (Fig. 4g), two peaks were observed at 531.39 eV and 532.82 eV, which were assigned to C=O and O–C=O, and –C–O and O–H bonds⁴⁸. Moreover, the peaks were higher than the typical peak of 530 eV, indicating nanohybrid formation⁴⁷. Figure 4h displays the XPS short scan spectrum for N 1s, and it shows three peaks at 398.75 eV, 399.53 eV, and 400.34 eV, showing the sp³-C–N, –NH₂ and O=CH–NH bonds present in the base polymer of the nanocomposite, respectively⁴⁹. Since there was a slight change in the binding energy of C 1s, O 1s, and N 1s, it was inferred that the self-assembly of Cd/CdIn₂S₄ on the chitosan surface might be due to chemical interactions. Although, there are some chances of physical interactions, which may be due to the hydrophobic interaction of the active molecules.

Elemental mapping

The uniform distribution of the components Cd, In, S, C, N, and O in the produced composite is confirmed by the element mapping (Supplementary Fig. 1b), which is an exact match to the EDX data and suggests that CdIn₂S₄ has grown on chitosan nanosheets.

These components are evenly distributed, which indicates that Cd/CdIn₂S₄@Ch quantum dots are distributed evenly. This conclusion supports the creation of an efficient inorganic–organic hybrid heterojunction between the organic chitosan matrix and inorganic CdIn₂S₄ to form evenly spread quantum dots³⁸.

FTIR analysis

FTIR technique was employed to analyze the functional groups in chitosan, CdIn₂S₄, and Cd/CdIn₂S₄@Ch quantum dot surfaces. As seen in Supplementary Fig. 1c, the FTIR spectrum of CdIn₂S₄ does not show any significant peaks in the IR region, suggesting the absence of any organic functional groups and the high purity of the sample. However, the FTIR spectrum of chitosan and Cd/CdIn₂S₄@Ch was almost similar and revealed a strong band in the range of 3650 to 3000 cm⁻¹, which was accredited to the stretching of N–H and O–H bands overlapping in the same region⁵⁰. Two small bands at around 2952 cm⁻¹ and 2871 cm⁻¹ are the characteristic bands of naturally occurring polysaccharides and are generally found in xylan and glucans, corresponding to symmetric and asymmetric stretchings of C–H bonds, respectively⁵¹. The bands at 1650 cm⁻¹ (C=O stretching) and 1320 cm⁻¹ (C–N stretching) confirm the presence of *N*-acetyl groups. The N–H bending, which is one of the characteristic bands of the amide groups, was confirmed by a small band at around 1552 cm⁻¹. The bands at 1425 cm⁻¹ and 1375 cm⁻¹ correspond to CH₂ bending and CH₃ symmetrical vibrations⁵². The chitosan's asymmetric stretchings of C–O–C bridges were attributed to the absorption band at 1150 cm⁻¹. Two small peaks at 1060 cm⁻¹ and 1026 cm⁻¹ were attributed to the stretchings of C–O bonds. The final small band at 895 cm⁻¹ corresponds to the out-of-plane bending of C–H bonds in the monosaccharide rings. All the bands in the FTIR spectrum are in good agreement with the previously reported studies⁵³.

Photocatalytic experiment

Primarily an oxidant, hydrogen peroxide plays a critical part in the photo-Fenton-like oxidation process⁵⁴. The visible light irradiation upon H₂O₂ produces •OH radicals in addition to reacting with the catalyst to yield them. Thus, it is essential to study and investigate its effect on the photodegradation of ofloxacin and para-nitrophenol using the fabricated quantum dots. To achieve this goal, the hydrogen peroxide was varied from 2 μL mL⁻¹ to 10 μL mL⁻¹, i.e., 0.1–0.5 mL of H₂O₂ in a 50 mL solution of 20 ppm of ofloxacin and 15 ppm para-nitrophenol. The photodegradation efficiency and kinetic rate constant due to the presence of hydrogen peroxide are presented in Supplementary Table 2. As can be perceived in Fig. 5a, c, an upsurge in the photocatalytic activity was observed until 4 μL mL⁻¹ and 6 μL mL⁻¹ for ofloxacin and para-nitrophenol, respectively, while a significant decrease was observed after increasing the peroxide dosage. The initial increase can be ascribed to the self-decomposition of H₂O₂ due to irradiation of visible light into •OH radicals (Eq. 6), and the decrease in efficiency for increased peroxide dosage may be due to the self-scavenging of •OH radicals by excess H₂O₂ (Eq. 7)⁵⁵.



Moreover, the photocatalyst also contributes to creating •OH radicals in the presence of visible light⁵⁶. Equations (8–11) suggest that the fabricated Cd/CdIn₂S₄@Ch quantum dots produce e⁻ and h⁺ upon visible light irradiation, which then reacts with peroxide molecule and hydroxyl ion to form •OH radicals. H₂O₂ doses of 0.2 mL and 0.3 mL resulted in degradation efficiency of 82.01 ± 1.72% and 92.48 ± 1.67% for ofloxacin and para-

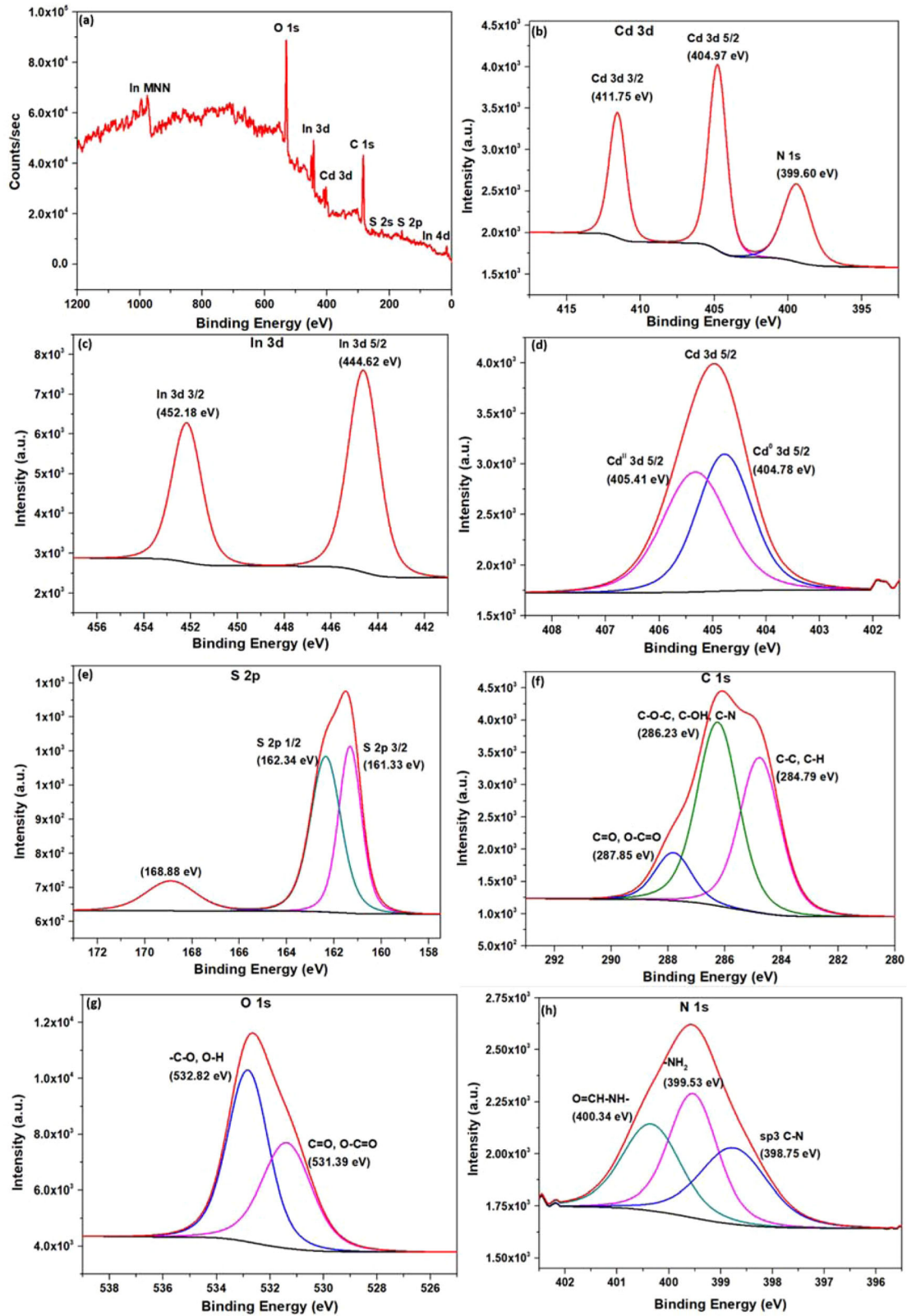


Fig. 4 XPS analysis of Cd/CdIn₂S₄@Ch quantum dots. **a** Survey spectrum: short scan spectra of **(b)** Cd 3d, **(c)** In 3d, **(d)** Cd 3d_{5/2}, **(e)** S 2p, **(f)** C 1s, **(g)** O 1s, and **(h)** N 1s.

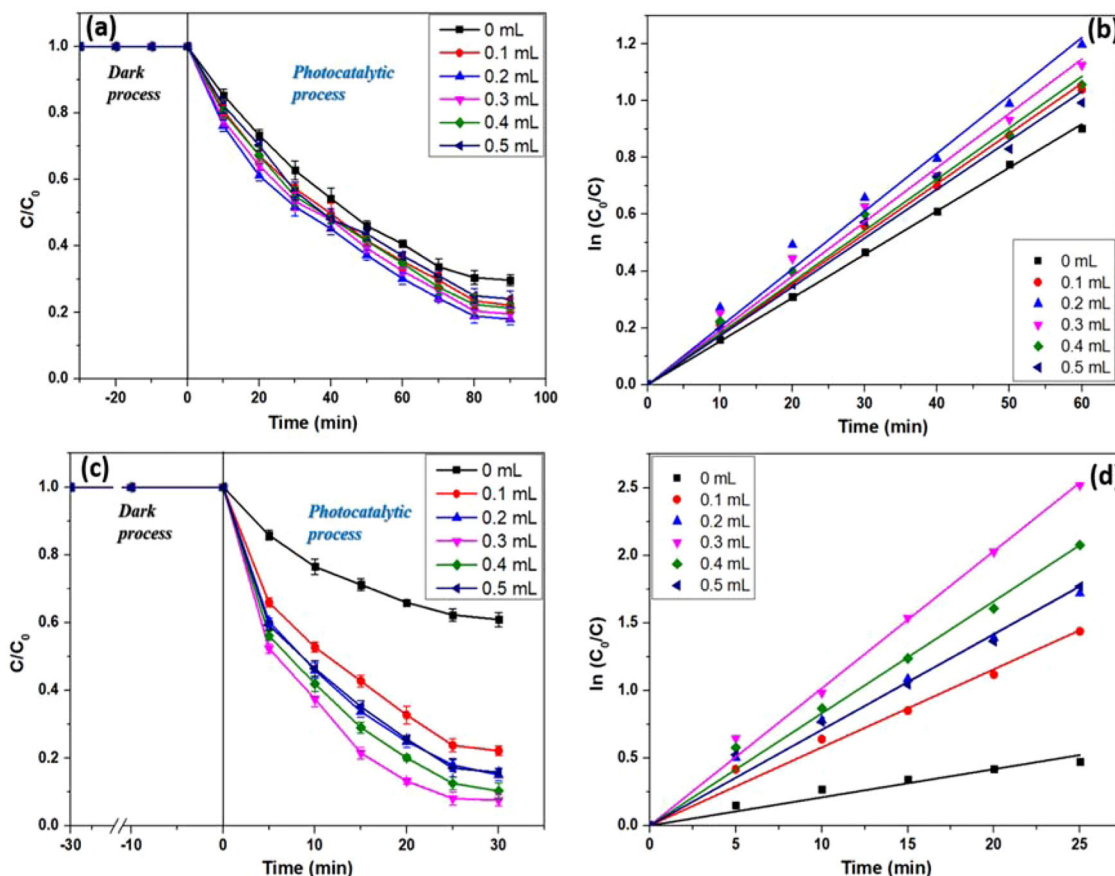


Fig. 5 Influence of H_2O_2 dosage on degradation performance of Cd/CdIn $_2$ S $_4$ @Ch quantum dots. Effect of H_2O_2 dosage on the photodegradation of (a) ofloxacin and (c) para-nitrophenol; degradation kinetics for (b) ofloxacin and (d) para-nitrophenol; Reaction conditions: OFL/PNP concentration—20/15 ppm; catalyst dosage—8/8 mg; pH—7/7; H_2O_2 dosage—0–0.5 mL. Error bars represent the standard deviations.

nitrophenol, respectively, with pseudo-first-order specific reaction rates of 0.02038 and 0.10153 min^{-1} (Fig. 5b, d).



The pH of the solution is greatly determined by the surface charge of the synthesized Cd/CdIn $_2$ S $_4$ @Ch quantum dots. The initial optimum pH must be calculated together with the types of pollutants present in the wastewater to maximize the degradation of contaminants in wastewater⁵⁷. For this, the pH at Zero Point Charge (ZPC) was determined by varying the pH from 3 to 11 utilizing 0.1 M NaOH and HCl in 0.01 M KNO $_3$ electrolyte solution through the Dynamic Light Scattering (DLS) technique. The pH-ZPC value was found to be 6.31 when 0.01 g of Cd/CdIn $_2$ S $_4$ @Ch was used. pH is the most vital parameter that impacts the performance of catalytic photodegradation, as the efficiency of fabricated Cd/CdIn $_2$ S $_4$ @Ch is affected by the solution's pH. Prior to visible light irradiation, the pH of the solution is adjusted; the pH is not monitored as the reaction progresses. As shown in Supplementary Table 3, a pH range of 3 to 11 was utilized to study the influence of pH on the degradation of ofloxacin and para-nitrophenol.

The initial concentration of ofloxacin was fixed at 20 ppm, while the catalyst dose was kept at 8 mg for 50 mL of solution alongside

0.2 mL of H_2O_2 . It was seen that the optimum pH was 7, as it showed a maximum degradation efficiency of $82.01 \pm 1.72\%$ with a rate constant of 0.02038 min^{-1} . An upsurge in efficiency was observed till pH 7, and after that, a decrease in performance was noticed (Supplementary Fig. 2a, b). Because nitrogen is present in position 4 of the piperazinyl group, ofloxacin is cationic below $\text{pK}_{a1} = 6.05$, anionic above $\text{pK}_{a2} = 8.11$ (due to the 6-carboxyl group), and zwitterionic, meaning neutral, within pK_{a1} and pK_{a2} ⁵⁸. The influence of the pH of the ofloxacin solution cannot be explained in terms of the ionization state of the catalyst and the substrate, as both the catalyst and the substrate transmit either negative or positive charges at alkaline or acidic conditions, accordingly, in catalytic photodegradation⁵⁹. At low pH levels, positive holes are the primary oxidation species, but at neutral or high pH values, $\bullet\text{OH}$ radicals are the primary oxidation species⁶⁰. Thus, considering the data from Supplementary Table 3 and the surplus of $\bullet\text{OH}$ radicals due to peroxide, the oxidative transformation of ofloxacin is mainly due to radicals rather than valence bond holes.

The influence of pH on the catalytic photodegradation of para-nitrophenol was tested utilizing 15 ppm of it using 8 mg of catalyst in 50 mL of solution with 0.3 mL of hydrogen peroxide. As the pH increases from 3 to 11, the degradation efficiency of the fabricated Cd/CdIn $_2$ S $_4$ @Ch quantum dots decreases (Supplementary Fig. 2c, d). The optimum pH was 3, with a maximum degradation efficacy of $94.72 \pm 1.47\%$ and a pseudo-first-order specific rate constant of 0.1058 min^{-1} . The decline in efficiency with increasing pH may be attributed to the production of OH^- ion, which may quench the production of $\bullet\text{OH}$ radicals by reacting

with it. The H_2O_2 breakdown reaction was also stimulated at a lower pH to generate $\cdot\text{OH}$ radicals in the solution, while the free radicals' recombination reaction rate decreased⁶¹.

The reaction's initial contaminant concentration, H_2O_2 dosage, and pH were set at 20 and 15 ppm, 0.2 and 0.3 mL, and 7 and 3, respectively, to examine the effects of the catalyst dose on the photodegradation of ofloxacin and para-nitrophenol. The photocatalyst dosage varied from 4 to 16 mg in 50 mL of solution or from 0.08 to 0.32 g L^{-1} . The photodegradation was discovered to increase with increasing photocatalyst amounts, peaking at 10 mg (0.2 g L^{-1}) and 12 mg (0.24 g L^{-1}) for ofloxacin and para-nitrophenol, respectively, before showing a modest fall (Supplementary Fig. 3a, c). It is feasible to attribute an initial upsurge in catalytic efficiency with an increase in catalyst dosage to an expansion in active sites brought on by introducing the photocatalyst. Nevertheless, as more catalyst was added, photons could not enter the suspension deeply. The photocatalytic effectiveness somewhat decreased due to increased solution opacity that caused light to scatter⁵⁵. In addition, due to the presence of hydrogen peroxide, an increase in the photocatalyst dosage amplified the production of $\cdot\text{OH}$ radicals, yet excess $\cdot\text{OH}$ radicals may endure recombination at a high catalyst dosage⁶². Thus, it can be concluded that photocatalyst optimization is essential as it reduces the excessive use of the catalyst. As shown in Supplementary Table 4, the optimized dosage resulted in the maximum degradation efficiency of $85.51 \pm 1.35\%$ and $96.70 \pm 1.31\%$ for ofloxacin and para-nitrophenol, respectively, with pseudo-first-order specific rate constants of 0.02334 and 0.15134 min^{-1} (Supplementary Fig. 3b, d).

The initial pH was set at 7 and 3, the catalyst loading was maintained at its optimal level of 0.2 and 0.24 g L^{-1} , the hydrogen peroxide dose at 0.2 and 0.3 mL, and the initial concentration of the contaminants was kept varying from 10 ppm to 40 ppm to study the effects of the initial concentration of ofloxacin and para-nitrophenol, respectively (Table 1). Ofloxacin and para-nitrophenol have a range of concentrations in water bodies between $\mu\text{g L}^{-1}$ and mg L^{-1} , although these high beginning concentrations are frequently employed in photodegradation investigations to ensure accurate concentration evaluation and identification of transformation products during the photodegradation process. After an initial increase in the concentration of ofloxacin and para-nitrophenol, a minor increase in photodegradation efficiency was observed up to 20 and 15 ppm, respectively, after which a slight fall was recorded (Fig. 6a, c). The narrowing of photon path lengths may be principally responsible for the minor decrease in the photodegradation of the pharmaceutical and phenol with further increases in its concentration⁶³. Additionally, higher initial contaminant concentrations would necessitate a heavier catalyst load, enhancing the solution's opacity and inevitably inhibiting photodegradation⁶⁴. Likewise, as the concentrations of ofloxacin and para-nitrophenol rose, the pollutants took more active sites, gradually displacing surface-adsorbed OH^- ions and O_2 molecules. This phenomenon caused the photocatalyst to generate inadequate amounts of hydroxyl radicals ($\cdot\text{OH}$) and superoxide anion radicals ($\cdot\text{O}_2^-$), which had reduced overall efficiency by that time. As all the reaction parameters were optimized, the maximum degradation efficacy of ofloxacin and para-nitrophenol by Cd/CdIn₂S₄@Ch quantum dots was found to be $85.51 \pm 1.35\%$ and $96.70 \pm 1.31\%$, respectively, with pseudo-first-order rate constants of 0.02334 and 0.15134 min^{-1} (Fig. 6b, d).

The effect of exposure time was studied in optimal conditions for ofloxacin and para-nitrophenol at a catalyst dose of 10 mg and 12 mg and a contaminant concentration of 20 ppm and 15 ppm. As shown in Fig. 7a, b, every possible combination was tested to understand the photocatalytic activity over a certain period. It was inferred that no further decrease in the concentration of ofloxacin and para-nitrophenol was observed after 90 and 30 min, respectively. These outcomes can result from the depletion of the photocatalyst's active sites⁶⁵. The maximum photocatalytic degradation for synthesized Cd/CdIn₂S₄@Ch quantum dots in the

Table 1. Degradation performance at various initial concentrations.

Contaminant	Concentration (ppm)	Degradation efficiency (%)	Rate constant (min^{-1})	R^2
Ofloxacin	10	85.00 ± 1.58	0.02254	0.99699
	15	85.22 ± 1.11	0.02289	0.9964
	20	85.51 ± 1.35	0.02334	0.99549
	25	82.83 ± 2.14	0.02013	0.99702
	30	78.67 ± 1.49	0.01861	0.99832
	35	74.52 ± 2.11	0.01688	0.99911
	40	70.37 ± 1.97	0.01561	0.99903
Para-nitrophenol	10	95.77 ± 1.47	0.116	0.99427
	15	96.70 ± 1.31	0.15134	0.98307
	20	94.76 ± 1.18	0.11093	0.99253
	25	92.15 ± 2.17	0.10304	0.99124
	30	89.54 ± 1.93	0.0939	0.99376
	35	86.93 ± 1.24	0.08484	0.99301
	40	81.43 ± 2.43	0.07166	0.98817

presence of H_2O_2 for ofloxacin and para-nitrophenol was found to be $85.51 \pm 1.35\%$ and $96.70 \pm 1.31\%$, respectively. No changes in contaminant concentration were observed during photolysis, i.e., degradation in the absence of the photocatalyst or the presence of only peroxide. Figure 7c displays the degradation rate constant of the various systems, and it was observed that Cd/CdIn₂S₄@Ch quantum dots in the presence of H_2O_2 showed a pseudo-first-order rate constant of 0.02334 and 0.15134 min^{-1} for ofloxacin and para-nitrophenol, respectively.

Furthermore, as shown in Fig. 7d, e, the total COD was reduced by $80.67 \pm 1.67\%$ and $88.36 \pm 1.43\%$ from their initial values of 720 mg $\text{O}_2 \text{L}^{-1}$ and 135 mg $\text{O}_2 \text{L}^{-1}$, respectively, for 20 ppm of ofloxacin and 15 ppm of para-nitrophenol. The degradation of these pollutants produces aromatic intermediates that can be found by HR-LCMS analysis. These intermediates probably shielded the enormous number of ROSs created during photocatalysis, which could have inhibited the solution's COD percentage from dropping further⁶⁶. The optimized catalyst was also used to degrade other organic compounds, such as dyes and pharmaceuticals like Methylene blue (MB), Crystal Violet (CV), Congo red (CR), Ranitidine (RNT), Amoxicillin (AMO), and Sulfamethoxazole (SMZ). The contaminant's concentrations were 20 ppm and were degraded at pH 7 with a catalyst dose of 10 mg. Therefore, a slight decline in the degradation efficacy of para-nitrophenol was observed as the pH was slightly higher than the optimal pH. The degradation competence followed the order CV ($97.31 \pm 1.56\%$) > MB ($96.23 \pm 2.1\%$) > PNP ($92.48 \pm 1.67\%$) > CR ($90.33 \pm 1.33\%$) > OFL ($85.51 \pm 1.35\%$) > RNT ($73.22 \pm 1.89\%$) > SMZ ($53.89 \pm 2.47\%$) > AMO ($42.36 \pm 2.66\%$). Although the fabricated Cd/CdIn₂S₄@Ch quantum dots showed very high degradation efficiency for dyes, this paper focused on removing the toxic emerging pollutants (ofloxacin and para-nitrophenol) after thoroughly going through the research gaps (Fig. 7f). Moreover, it is safe to say that the synthesized photocatalyst is efficient in removing nearly all types of pollutants and can be used in real water applications.

The effect of temperature on the photodegradation efficiency is also investigated under optimal conditions, with the temperatures varying from 25 °C to 40 °C. As illustrated in Supplementary Fig. 4a, c, the photocatalytic performance of Cd/CdIn₂S₄@Ch narrowly decreases with an increase in temperature for both ofloxacin and para-nitrophenol. Although the frequency of collisions initially rises with temperature as performance grows with time, this only accounts for a tiny portion of the increase in reaction rate⁶⁷. The

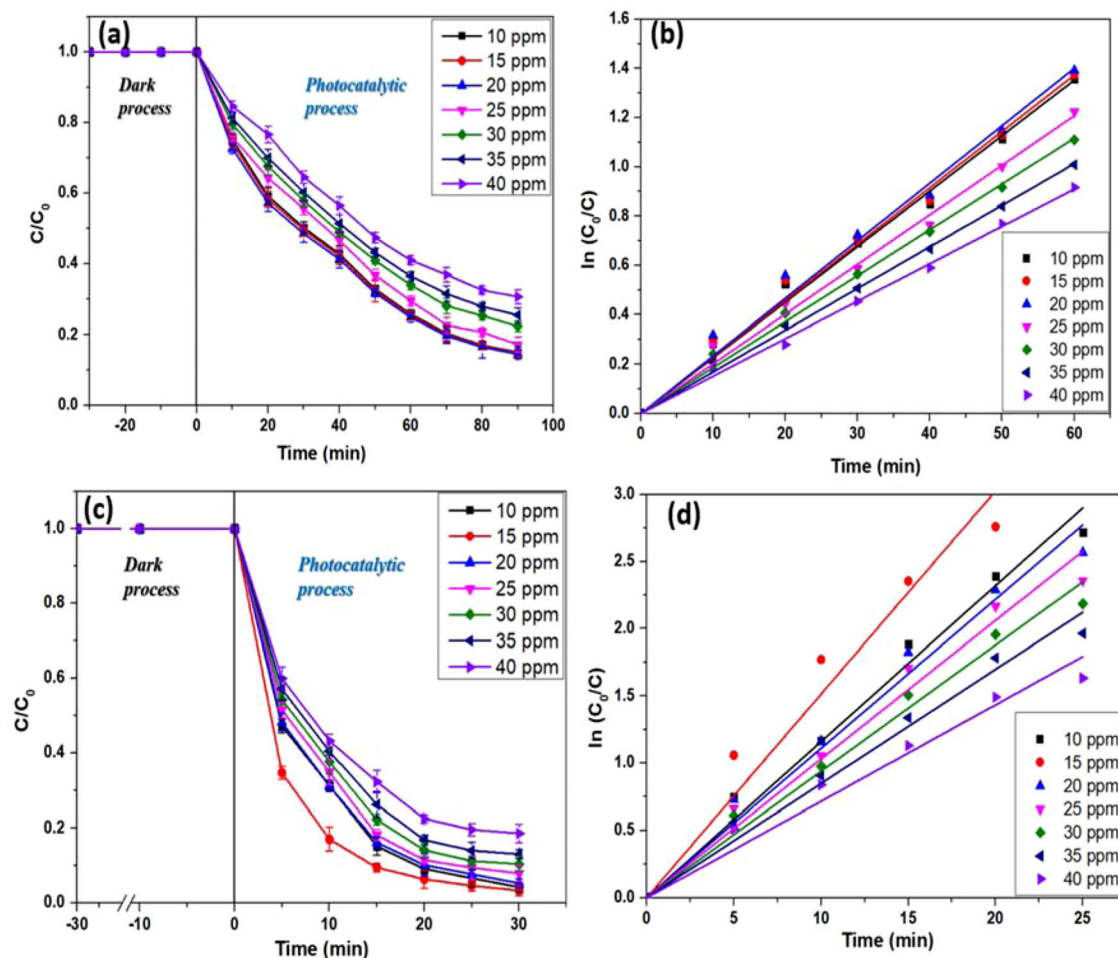


Fig. 6 Influence of contaminant concentration on degradation performance of Cd/CdIn₂S₄@Ch quantum dots. Effect of initial contaminant concentration on the photodegradation of (a) ofloxacin and (c) para-nitrophenol; degradation kinetics for (b) ofloxacin and (d) para-nitrophenol; Reaction conditions: OFL/PNP concentration—10–40 ppm; catalyst dosage—10/12 mg; pH—7/3; H₂O₂ dosage—0.2/0.3 mL. Error bars represent the standard deviations.

low adsorption of the pollutants on the surface of the nanocomposite is caused by the high kinetic energy, which overshadows the beneficial impact of higher collision frequency. This causes the generated ROS to recombine, which lowers the degradation performance⁶⁸. Supplementary Fig. 4b, d display the reduction in degradation rate, which is further summarized in Supplementary Table 5.

Furthermore, the photodegradation efficiency was significantly reduced in other combinations, such as pristine CdIn₂S₄ in the presence of H₂O₂, Cd/CdIn₂S₄@Ch, and CdIn₂S₄ in the absence of H₂O₂ (Supplementary Fig. 5a). The studies of the photodegradation of ofloxacin and para-nitrophenol showed that the relatively quick recombination of photoinduced e⁻ and h⁺ might be the cause of the subpar photocatalytic efficiencies, which the photoluminescence spectroscopy can confirm (Fig. 1d). A practical and crucial method for improving the photocatalytic performance of Cd/CdIn₂S₄@Ch quantum dots was to include oxidants, such as hydrogen peroxide, as electron acceptors in the reaction to lower the likelihood of charge carrier recombination because the oxidants immediately trapped photogenerated electrons⁶⁹. In addition, the TOC removal efficiency for ofloxacin and para-nitrophenol in different systems was also analyzed (Supplementary Fig. 5b). The Cd/CdIn₂S₄@Ch quantum dots showed the highest mineralization in the presence of H₂O₂, with an efficiency of 73.49% and 86.34% for ofloxacin and para-

nitrophenol, respectively, in the optimized conditions. Such high mineralization efficiency can be supported through HR-LCMS analysis, showcasing the breakdown of complex contaminant molecules into smaller ones. Furthermore, quantum yield (Supplementary Fig. 5c) and figure of merit (FoM) (Supplementary Fig. 5d) measurements were used to assess the parallel performance of the photocatalysts in the presence and absence of H₂O₂. Quantitative measurements of a photocatalyst's effectiveness at absorbing irradiation photons and using them to destroy the target pollutant are known as quantum yield⁷⁰. Additionally, the FoM parameter was generated for each catalyst using various process parameters to realistically analyze the actual performances of these photocatalytic systems, given the variations in the conversion efficiency values⁷¹. Thus, it was concluded that the Cd/CdIn₂S₄@Ch quantum dots showed the maximum quantum yield and FoM of 8.13×10^{-5} molecules photon⁻¹ and 2.065×10^{-4} , and 5.38×10^{-4} molecules photon⁻¹ and 7.78×10^{-4} for ofloxacin and para-nitrophenol, respectively, in the presence of hydrogen peroxide, compared to a low quantum yield and FoM of 6.71×10^{-5} molecules photon⁻¹ and 1.69×10^{-4} , and 2.16×10^{-4} molecules photon⁻¹ and 3.14×10^{-4} , in the absence of hydrogen peroxide.

The degradation of ofloxacin and para-nitrophenol in the existence of inorganic ions, organic compounds, and various water matrices was investigated to support the earlier claim. As

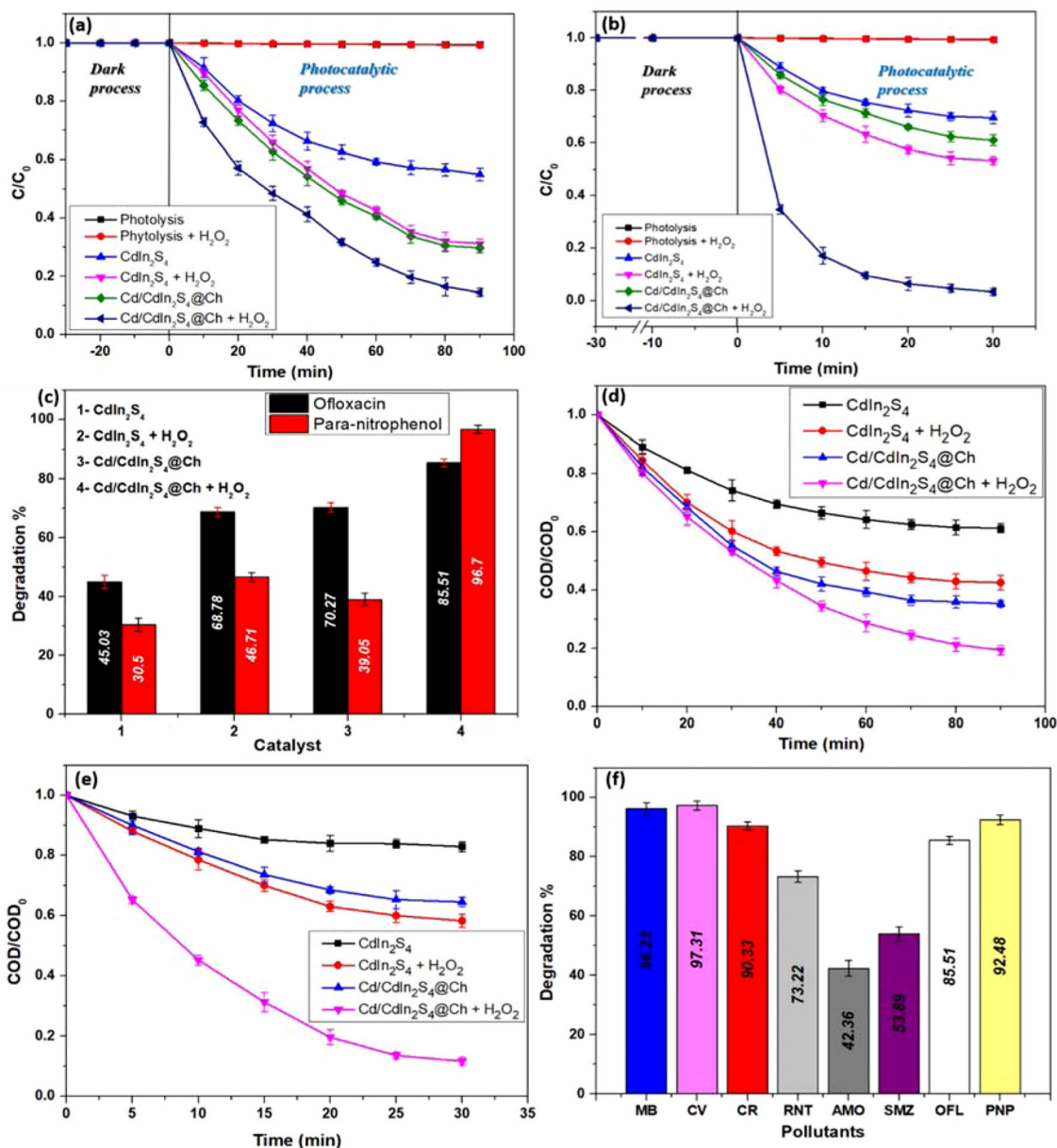


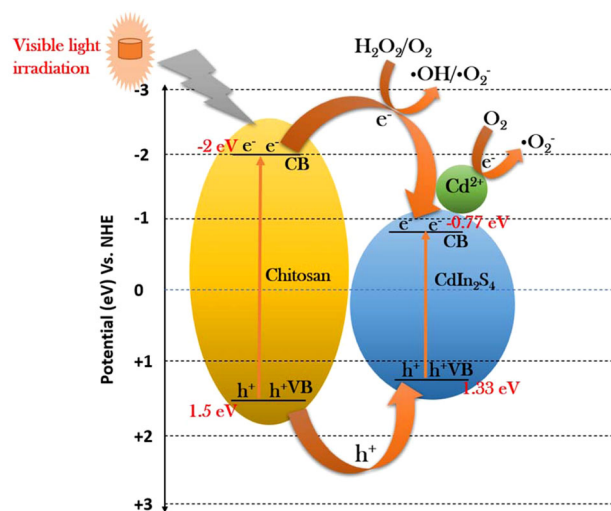
Fig. 7 Degradation performance of the fabricated photocatalysts at various reaction conditions. Effect of contact time on the photodegradation of (a) ofloxacin and (b) para-nitrophenol; (c) degradation performance by various catalyst combinations; COD analysis for the degradation of (d) ofloxacin and (e) para-nitrophenol; (f) degradation performance of Cd/CdIn₂S₄@Ch quantum dots on various other pollutants; Reaction conditions: OFL/PNP concentration—20/15 ppm; catalyst dosage—10/12 mg; pH—7/3; H₂O₂ dosage—0.2/0.3 mL. Error bars represent the standard deviations.

discussed in the comparison of the Cd/CdIn₂S₄@Ch quantum dots with recently published works in Table 2, these two contaminants were degraded previously, but our catalyst showed excellent efficiency at even low catalyst dose and visible light irradiation. It is well known that the volume of photogenerated ROSs, electrons, and holes directly affects the rate of an AOP-assisted photocatalytic degradation process⁷². To confirm which one of them had a major role in the degradation of ofloxacin and para-nitrophenol in the aqueous phase, some sacrificial agents were added during the degradation experiment to trap them. This study allowed for a proper and thorough assessment of the role played by the reactive species such as •OH (hydroxyl), •O₂⁻ (superoxide), e⁻ (electron), and h⁺ (hole). Benzoic acid as •OH scavengers, Benzoquinone as •O₂⁻ scavengers, Potassium persulfate (K₂S₂O₈) as e⁻ scavengers, and

Disodium EDTA as h⁺ scavengers were used. Benzoic acid and Benzoquinone restrict the performance of the degradation of pharmaceutical and phenolic compounds as they scavenge the hydroxyl and superoxide radicals, respectively⁷³. Moreover, scavenging electrons and holes through K₂S₂O₈ and Disodium EDTA would decrease the formation of •OH radicals, thus reducing the overall effectiveness. In the case of ofloxacin degradation (Supplementary Fig. 6a), •OH (hydroxyl) and •O₂⁻ (superoxide) radical scavengers would decline their efficiency to 25.97 ± 2.17% and 32.08 ± 1.99%, respectively, whereas for para-nitrophenol (Supplementary Fig. 6b), the efficiency would slump down to 35.21 ± 1.89%, and 40 ± 2.19%. However, K₂S₂O₈ and Disodium EDTA had a minor impact on the photocatalytic performance of fabricated Cd/CdIn₂S₄@Ch quantum dots for the degradation of ofloxacin and para-nitrophenol. Thus, this study

Table 2. Degradation performance of various other photocatalysts.

Pollutants	Catalyst	Pollutant Conc. (ppm)	Catalyst dosage (g/L)	Time (min)	Light Source	Efficiency (%)	Ref.
Ofloxacin	CdS/TiO ₂	5	0.45	180	Visible	86	108
	BaTiO ₃ /WS ₂	20	1	75	Visible	~90	109
	BPQDs/OV-BiOBr	10	1	90	300 W Xe-lamp	98.7	110
	BiOCl/BiOBr-Bi ₂₄ O ₃₁ Br ₁₀	50	1	180	400 W halogen lamp	78.3	111
	Gd ₂ Ti ₂ O ₇ /SiO ₂	20	0.4	90	20 W UV lamp	79.1	112
	Cd/CdIn ₂ S ₄ @Ch	20	0.2	90	23 W white LED	85.51 ± 1.35	This work
Para-nitrophenol	Co-Fe PBA	20	1	60	Dark/PMS-AOP	90	113
	rGO-ZnO	30	-	30	Plasma	87.6	114
	Fe ₃ O ₄	45	1.5	600	Visible	90	115
	TiO ₂	50	2	-	Gamma Radiation	~98	90
	Cd/CdIn ₂ S ₄ @Ch	15	0.24	30	23 W white LED	96.70 ± 1.31	This work

**Fig. 8 Plausible degradation mechanism.** Schematic representation of the photodegradation mechanism of ofloxacin and para-nitrophenol by fabricated Cd/CdIn₂S₄@Ch quantum dots.

provided sufficient information on the critical roles of the ROSs, •O₂⁻ and •OH, in the degradation of ofloxacin⁷⁴ and para-nitrophenol⁷⁵ while also illuminating the minor involvement of e⁻ and h⁺.

Degradation mechanism

The schematic representation of the degradation mechanism of toxic pollutants, such as ofloxacin and para-nitrophenol, under the influence of visible light, is illustrated in Fig. 8. When the photocatalyst was introduced to visible light, the electron was excited from the VB to the CB, producing holes (h⁺). The PL analysis confirms that the dopant serves as an electron scavenger and suppresses recombination between electrons and holes when illuminated by visible light (Fig. 1d). The photocatalytic ability was substantially enhanced when the electron-hole pair was prevented from recombining⁷⁶. Meanwhile, the CB and VB potentials can be calculated using the following Eqs. 12 and 13.

$$E_{CB} = \chi - E^e - 0.5 \times E_g \quad (12)$$

$$E_{VB} = E_{CB} + E_g \quad (13)$$

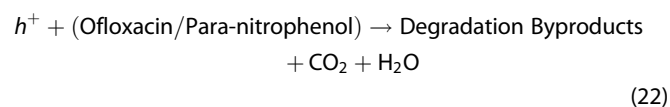
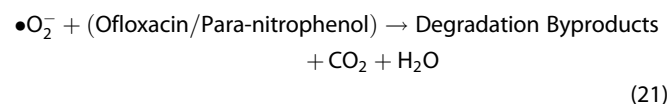
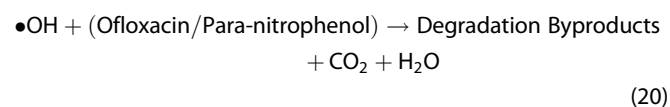
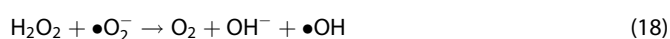
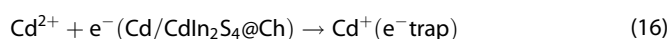
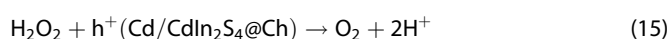
The χ value for Chitosan and CdIn₂S₄ was 4.2 and 4.97, respectively^{77,78}. The E_g value of CdIn₂S₄ was determined to be 2.1 eV through the UV-DRS analysis (Fig. 1d) from the curve of $(\text{ahv})^{1/2}$ vs. $h\nu$ plot, while for chitosan, the value was 3.5 eV, obtained from the previous literature⁷⁹. Hence, the calculated value of E_{CB} and E_{VB} for CdIn₂S₄ was -0.77 and 1.33 eV, whereas, for chitosan, the values were -2 and 1.5 eV, respectively. The CB and VB edge sites of CdIn₂S₄ were encapsulated in the chitosan energy gap and had notable characteristics of type-I heterojunction.

Based on the ROSs obtained from the scavenger experiment mentioned above and the bandgap analysis from UV-DRS, the charge transfer mechanism was projected for the photodegradation of ofloxacin and para-nitrophenol. Due to their superior visible light capturing abilities, chitosan and CdIn₂S₄ are activated by visible light to produce photoinduced electrons (e⁻) on CB and holes (h⁺) on VB. The h⁺ produced in the VB of chitosan and CdIn₂S₄ cannot react with the H₂O or OH⁻ in the solution; that is, they do not form •OH radical and eventually accumulate on the VB because the VB potentials of chitosan (+1.5 eV/NHE) and CdIn₂S₄ (+1.33 eV/NHE) cannot reach the potential required to form •OH, ($\text{•OH}/\text{H}_2\text{O} = +1.99$ eV/NHE, $\text{•OH}/\text{OH}^- = +2.40$ eV/NHE)⁸⁰. Thus, it was inferred that •OH radicals were not generated due to holes by the fabricated Cd/CdIn₂S₄@Ch quantum dots.

Because the VB potential of chitosan is more positive than the VB potential of CdIn₂S₄ and the CB potential of chitosan is more negative than the CB potential of CdIn₂S₄ in the heterostructure, e⁻ on the CB of chitosan can move to the CB of CdIn₂S₄ through the action of the internal electric field, and h⁺ generated on the VB of chitosan can move to the VB of CdIn₂S₄. The type-I photoinduced charge migration mechanism can significantly increase the separation efficacy of produced electron-hole pairs at the heterojunction interface, even though the photogenerated e⁻ and h⁺ on chitosan are transported to CdIn₂S₄ at a variable migration rate⁸¹. The e⁻ on the CB of CdIn₂S₄ can blend with O₂ and react to create •O₂⁻, as •O₂⁻ can directly react with the pollutants because the CB potential of CdIn₂S₄ is more negative than that of O₂/•O₂⁻ (-0.33 eV/NHE)⁸². Additionally, the harmful ofloxacin and para-nitrophenol could be immediately oxidized by the h⁺ on the VB of CdIn₂S₄.

Cd²⁺ traps electrons from the CdIn₂S₄ conduction band and changes them into Cd⁺. Due to its extreme instability, the Cd⁺ ion interacts with an oxygen molecule to form the superoxide radical (•O₂⁻)⁸³. According to Zhang et al.⁸⁴, cadmium exhibits a +2 oxidation state and a complete and stable electronic structure of 4d¹⁰. The stable electronic configuration of Cd²⁺ is distributed as

the electron is trapped by it. In order to create superoxide radicals, the trapped electron eventually moved to an oxygen molecule. Moreover, the cadmium ion does not trap holes as it disturbs the electronic configuration; instead, the holes react with the OH⁻ ion to form •OH radical⁷⁶. Furthermore, to improve the concentration of •OH radical, H₂O₂ was introduced to the degradation system. H₂O₂ is an electron-trapping agent, and it reacts with the electrons shifting from the CB of chitosan to CdIn₂S₄, forming •OH radical. The capture of e⁻ also leads to the increased speed of charge carrier transfer. However, excess H₂O₂ may waste other ROSs and reduce the degradation efficiency of ofloxacin and para-nitrophenol. Thus, the peroxide dosage was optimized to find the exact amount to be used in the degradation system. Equations (6–8), (10), and (14–22) show the reaction processes under visible light illumination:



HR-LC-MS analysis

An HR-LC-MS investigation was carried out to look into potential degradation pathways and intermediates for the breakdown of ofloxacin and para-nitrophenol, as described in Table 3. Three plausible pathways and 18 intermediate transformation products (OFL1–18) were proposed for ofloxacin, as shown in Fig. 9. Pathway 1 started with defluorination and breakdown of the morpholine ring, followed by decarboxylation and reduction to obtain OFL5 ($m/z = 233$)⁸⁵. Additionally, ring cleavage and opening took place, causing the larger molecule to split into the smaller molecules OFL8 ($m/z = 69$) and OFL9 ($m/z = 118$), followed by mineralization of these molecules into carbon dioxide, water, and other by-products. In pathway 2, defluorination occurred, OFL10 ($m/z = 358$), followed by the breakdown of molecules in two separate pathways leading to the formation of smaller aliphatic (OFL14; $m/z = 141$) and aromatic molecules (OFL13; $m/z = 85$)⁸⁶. Pathway 3 resulted in decarboxylation, followed by the removal of the piperazine ring, resulting in the production of OFL15 ($m/z = 218$), followed by defluorination, which led to the disintegration of the molecules into the smaller ring-like structure, OFL17 ($m/z = 110$) and OFL18 ($m/z = 97$)⁸⁷. The smaller molecules obtained from different pathways undergo mineralization to produce carbon dioxide, water, and other by-products⁸⁸.

Furthermore, para-nitrophenol degradation was proposed using three plausible pathways and 11 intermediate transformation

products (PNP1–11), as illustrated in Fig. 10. Pathway 1 showed the role of the •OH radicle, where the •OH radicle replaced NO₂ to produce PNP3 ($m/z = 110$). Additionally, the •OH radicle again attacks the molecule forming PNP5 ($m/z = 126$), leading to ring cleavage due to a growth in the electron density, resulting in the production of smaller molecules, PNP6 ($m/z = 85$) and PNP7 ($m/z = 60$), that further mineralized to carbon dioxide, water, and other-byproducts⁸⁹. In pathway 2, the •OH radicle attacks the ortho position of the para-nitrophenol, forming PNP8 ($m/z = 154$). Then, the molecule undergoes ring cleavage and further breakdowns into smaller molecules. Pathway 3 shows the reduction of para-nitrophenol to para-aminophenol, PNP11 ($m/z = 109$) due to the electrons and H⁺ ions present in the reaction mixture. Aromatic ring cleavage was believed to have complicated intermediates that may eventually be mineralized to CO₂ and H₂O or transformed into low molecular carboxylic acids like formic acid and oxalic acid. •OH radicals converted the nitrite created from the released nitro group into nitrate, forming several by-products⁹⁰.

Reusability

Its recyclability was examined to determine the prepared photocatalyst's reusability and stability (Fig. 11a, b). The photocatalyst had to be centrifuged apart for the following cycle, cleaned with ethanol and distilled water multiple times, and dried at 60 °C for 4 h. Figure 11c shows that the photocatalyst could be recycled six times in a row without experiencing a significant decrease in photocatalytic performance. The disruption of the chitosan polymer's porous structure and the obstruction of surface sites, however, may be the cause of a slight decline in degradation efficiency. The effective charge separation and support of the chitosan matrix play a significant role in the stability of the Cd/CdIn₂S₄@Ch photocatalyst. It was pretty astonishing to see that, even after six cycles, the synthesized quantum dots showed an excellent degradation performance of $60.79 \pm 1.74\%$ and $75.14 \pm 1.75\%$, indicating the photocatalyst's excellent reusability.

Additionally, the reused catalyst after 6 cycles was examined by TEM, EDX, and XRD analysis to determine the stability of Cd/CdIn₂S₄@Ch. The TEM images (Fig. 11d) of the catalyst after 6 cycles of degradation of ofloxacin and para-nitrophenol confirmed that the morphology had not been changed. Although the weight percentage of Cd and In slightly decreased in comparison to the fresh catalyst, the ratio of the elements remained intact, confirming the stability of the fabricated Cd/CdIn₂S₄@Ch quantum dots (Fig. 11e, f). In addition, no notable change in peaks of XRD of reused Cd/CdIn₂S₄@Ch was observed after the degradation of ofloxacin and para-nitrophenol, which indicated excellent stability of our fabricated quantum dots (Fig. 11g, h).

Effect of co-existing species (cations, anions, organic compounds, humic acid, salinity, sulfate ions) on the photodegradation of ofloxacin and para-nitrophenol

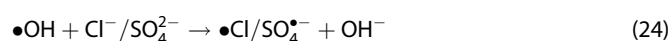
Various metal cations are present in wastewater or natural water; thus, the impact of their existence was examined using 0.01 M of Na₂SO₄, CaSO₄, and Al₂(SO₄)₃. The stable oxidation states of the metal salts, such as Na⁺, Ca²⁺, and Al³⁺, do not interfere with the photocatalytic process⁹¹. Figure 12a shows the degradation performance of the synthesized Cd/CdIn₂S₄@Ch quantum dots in the presence of monovalent, divalent, and trivalent cations. Photodegradation of ofloxacin was suppressed to varying degrees in the presence of the three salts. The sulfate ions of the salts could be responsible for the suppression in general due to their inhibitory effect. However, aluminum salt showed the most significant suppression of photocatalysis, i.e., $38.03 \pm 1.17\%$, probably due to Al³⁺ ions, as they prefer to adhere to the catalyst's surface. The active sites were blocked as a result of this affinity, which subsequently reduced the efficiency of the

Table 3. Intermediate transformation products obtained during the degradation of ofloxacin and para-nitrophenol.

Contaminant	Code	m/z value	Chemical formula	IUPAC Name
Ofloxacin	OFL1	362	C ₁₈ H ₂₀ FN ₃ O ₄	7-fluoro-2-methyl-6-(4-methylpiperazin-1-yl)-10-oxo-4-oxa-1-azatricyclo[7.3.1.0 _{5,13}]trideca-5(13),6,8,11-tetraene-11-carboxylic acid
	OFL2	306	C ₁₅ H ₁₈ N ₃ O ₄ ⁺	9-fluoro-3-methyl-10-(4-methylpiperazin-1-yl)-7-oxo-2,3-dihydro-7H-[1,4]oxazino[2,3,4-ij]quinoline-6-carboxylic acid
	OFL3	288	C ₁₅ H ₁₇ N ₃ O ₃	7-(4-methylpiperazin-1-yl)-4-oxo-1,4-dihydroquinoline-3-carboxylic acid
	OFL4	245	C ₁₄ H ₁₉ N ₃ O	1-(2-amino-4-(4-methylpiperazin-1-yl)phenyl)prop-2-en-1-one
	OFL5	233	C ₁₃ H ₁₉ N ₃ O	1-(2-amino-4-(4-methylpiperazin-1-yl)phenyl)ethanone
	OFL6	191	C ₁₁ H ₁₇ N ₃	3-(4-methylpiperazin-1-yl)aniline
	OFL7	151	C ₈ H ₁₃ N ₃	N ¹ -(2-aminoethyl)benzene-1,3-diamine
	OFL8	69	C ₄ H ₇ N	buta-1,3-dien-2-amine
	OFL9	118	C ₈ H ₇ N	1H-indole
	OFL10	358	C ₁₈ H ₂₀ N ₃ O ₅ ⁻	6-carboxy-3-methyl-10-(4-methylpiperazin-1-yl)-7-oxo-3,7-dihydro-2H-[1,4]oxazino[2,3,4-ij]quinolin-8-olate
	OFL11	155	C ₈ H ₁₃ NO ₂	(Z)-3-(3-methylmorpholino)acrylaldehyde
	OFL12	197	C ₁₁ H ₁₉ NO ₂	(Z)-4-methyl-5-(3-methylmorpholino)pent-3-enal
	OFL13	85	C ₄ H ₇ NO	3,6-dihydro-2H-1,4-oxazine
	OFL14	141	C ₈ H ₁₅ NO	(Z)-5-(ethylamino)-4-methylpent-3-enal
	OFL15	218	C ₁₂ H ₉ FNO ₂ ⁻	7-fluoro-2-methyl-6-(4-methylpiperazin-1-yl)-10-oxo-4-oxa-1-azatricyclo[7.3.1.0 _{5,13}]trideca-5(13),6,8,11-tetraene-11-carboxylic acid
	OFL16	201	C ₁₂ H ₁₁ NO ₂	3-methyl-2H-[1,4]oxazino[2,3,4-ij]quinolin-7(3H)-one
	OFL17	110	C ₆ H ₆ O ₂	hydroquinone
	OFL18	97	C ₅ H ₇ NO	2,3-dihydropyridin-4(1H)-one
Para-nitrophenol	PNP1	139	C ₆ H ₅ NO ₃	4-nitrophenol
	PNP2	154	C ₆ H ₄ NO ₄ ⁻	1-nitro-4-oxocyclohexa-2,5-dienolate
	PNP3	110	C ₆ H ₆ O ₂	4-hydroxycyclohexa-2,5-dienone
	PNP4	110	C ₆ H ₆ O ₂	hydroquinone
	PNP5	126	C ₆ H ₆ O ₃	hydroxyquinol
	PNP6	85	C ₄ H ₅ O ₂ ⁻	(Z)-4-oxobut-2-en-1-olate
	PNP7	60	C ₂ H ₄ O ₂	(Z)-ethene-1,2-diol
	PNP8	154	C ₆ H ₄ NO ₄ ⁻	2-hydroxy-5-nitrophenolate
	PNP9	153	C ₆ H ₃ NO ₄	4-nitrocyclohexa-3,5-diene-1,2-dione
	PNP10	125	C ₆ H ₇ NO ₂	N-hydroxy-N-phenylhydroxylamine
	PNP11	109	C ₆ H ₇ NO	4-aminophenol

photocatalytic reaction. Meanwhile, compared to Na⁺ which showed an efficiency of 55.08 ± 1.76%, Ca²⁺ showed higher suppression in photocatalytic ability, i.e., 51.77 ± 2.14%, presumably due to its larger size⁹².

0.01 M concentration of Cl⁻, F⁻, and SO₄²⁻ was introduced to understand the impact of various inorganic anions in the degradation ability of fabricated Cd/CdIn₂S₄@Ch quantum dots (Fig. 12b). A decrease in photocatalytic efficiency to 55.08 ± 2.13% and 54.01 ± 1.33% was observed upon introducing chlorine and sulfate anions, respectively. These anions reacted with the •OH radicals following second-order kinetics, thus quenching the photodegradation of ofloxacin and reducing its efficiency. In addition, when attached to the composite's surface, these anions react with the holes to produce chloride and sulfate radicals, which then react with the electrons to form back anion again, as shown in Eqs. 23–25 Iso⁹³, SO₄²⁻ anion slumped the photocatalytic ability even more than Cl⁻ anion due to its larger size.



On the other hand, fluoride ions are eminent because of their exceptional resistance to oxidation by holes⁹⁴. They are able to cover the photocatalyst's surface, which prevents the generation of surface •OH radicals. The upsurge in surface coverage of F⁻ ions with concentration was responsible for the observed decline in the photodegradation efficiency. The deterioration is, therefore, primarily fueled by accessible •OH radicals in the solution phase when F⁻ ion is present; thus, there is only a slight decrease in photodegradation efficiency (69.44 ± 2.84%).

Additionally, investigations were conducted to examine the role of organic compounds such as urea, humic acid sodium salt (HAS), and sodium dodecyl sulfate (SDS) on the photocatalytic degradation of ofloxacin. Urea is used as a beginning material for the production of polymers and medications and is used in fertilizers and feed additives⁹⁵. Both SDS, used in cleaning goods, and humic acids are typically found in wastewater⁹⁶. Therefore, it is vital to evaluate the effects of their presence on the ternary nano-photocatalytic photocatalyst's performance. As shown in Fig. 12c, SDS showed higher resistance to the degradation process among the three organic compounds. The creation of micelles around ofloxacin and the presence of SO₄²⁻ ions produced by the photolysis of SDS could be responsible for the SDS deactivation of photocatalysis. The competitive adsorption and inhibition by

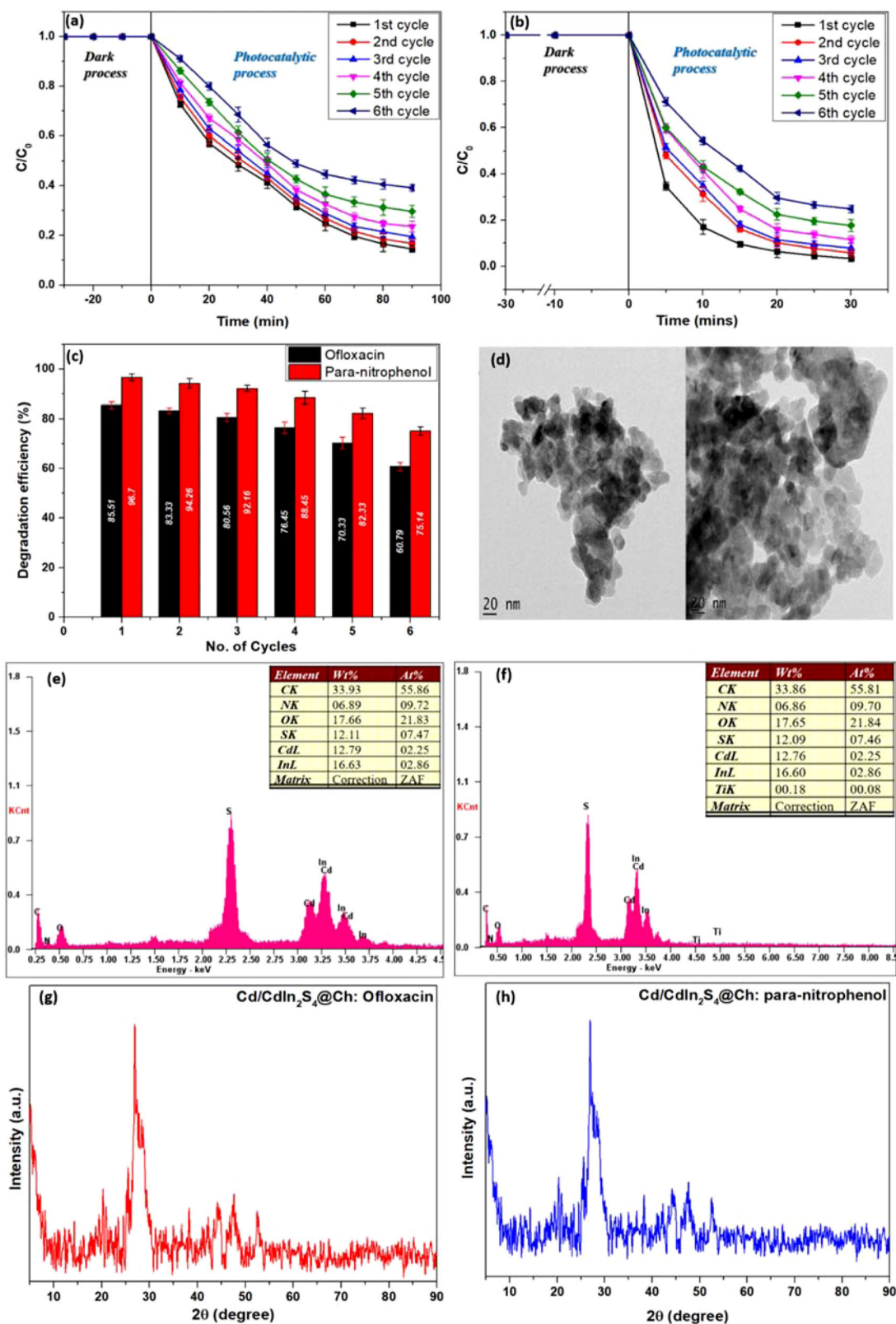


Fig. 11 Reusability and stability of Cd/CdIn₂S₄@Ch quantum dots. Reusability of Cd/CdIn₂S₄@Ch for the degradation of (a) ofloxacin and (b) para-nitrophenol; (c) degradation efficiency during various cycles; (d) TEM images, (e) and (f) EDX analysis, and (g) and (h) XRD spectra of Cd/CdIn₂S₄@Ch quantum dots after degradation of ofloxacin and para-nitrophenol, respectively. Error bars represent the standard deviations.

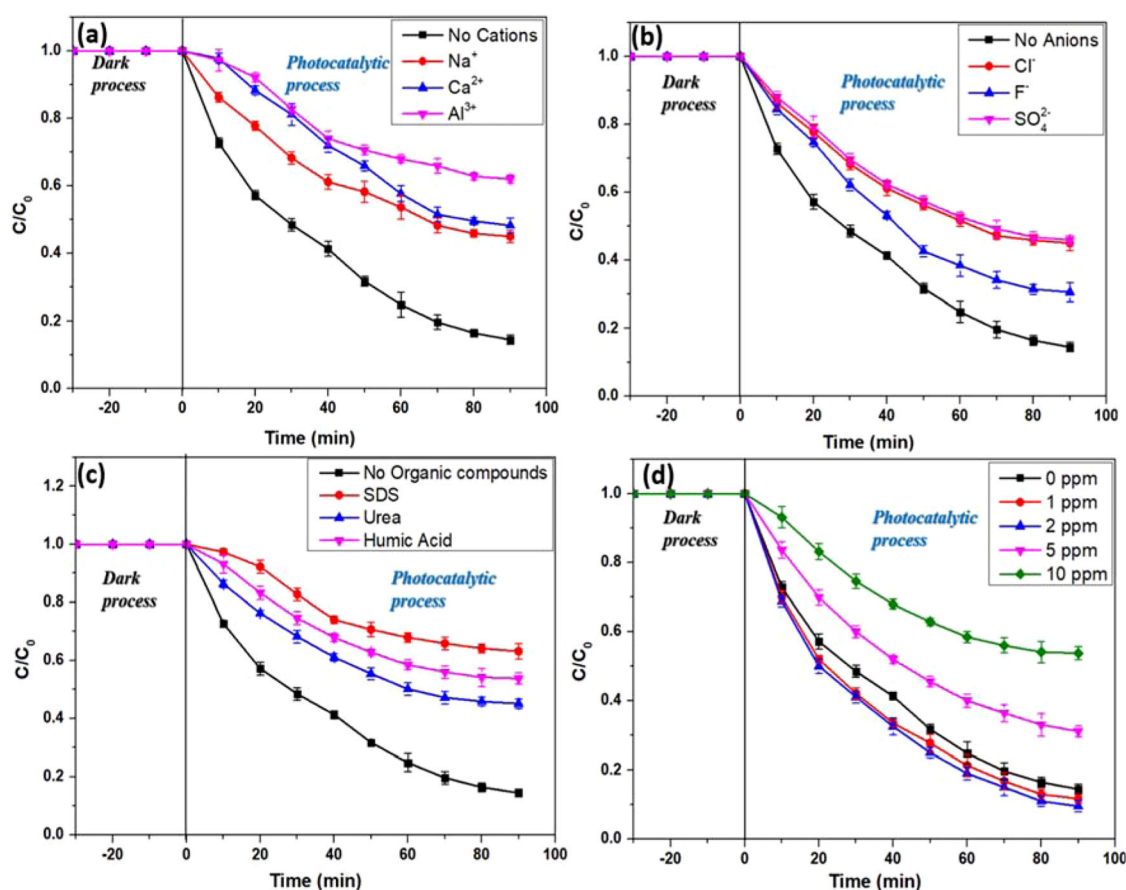


Fig. 12 Influence of co-existing species on ofloxacin removal by Cd/CdIn₂S₄@Ch quantum dots. Effect of (a) cations, (b) anions, (c) organic compounds, (d) humic acid on the photodegradation of ofloxacin; reaction conditions: OFL concentration—20 ppm; catalyst dosage—10 mg; pH—7; H₂O₂ dosage—0.2 mL. Error bars represent the standard deviations.

can be stimulated and produce radical species such as singlet oxygen (¹O₂) and the hydroxyl radical (radical •OH), which can break down target contaminants. The proportion of these two effects varies depending on the content of humic acid and the target pollutants, which impacts how the degradation by ionizing radiation is affected⁹⁷.

HAS solutions with 1, 2, 5, and 10 ppm concentrations were employed to degrade a 20 ppm 50 ml solution of ofloxacin in the presence of 0.2 ml H₂O₂. According to the study, the degradation efficiency increased to 88.31 ± 1.27% and 90.29 ± 1.76% for 1 and 2 ppm HAS concentrations. However, at 5 and 10 ppm, efficiency decreased to 68.89 ± 1.55% and 46.25 ± 1.93%, respectively. It can be derived that the elimination of organic contaminants in the presence of HAS is most likely dependent on the concentration of the organic contaminants because HA may improve their effectiveness in degradation at low concentrations while inhibiting degradation at higher concentrations through enhancing solution turbulence. This serves as one of the explanations for why its effect on organic compound elimination produces contradictory findings⁹⁸.

Figure 13a shows how the presence of sodium (Na⁺), calcium (Ca²⁺), and aluminum (Al³⁺) affects the photocatalytic degradation of para-nitrophenol. From Fig. 13a, it was interpreted that the cations had no impact on the photodegradation of para-nitrophenol apart from aluminum, which exhibited a slight reduction in the efficiency to 90.01 ± 2.12%. This result was due to the presence of sulfate anion, which then reacted with holes to form sulfate radical (SO₄^{•-}). Because of their capacity to oxidize phenol, these sulfonated radicals produce modest improvements

in the overall phenol degradation rate by producing reactive oxygen species. To further analyze the effect of anion on the degradation process, para-nitrophenol was photodegraded in the presence of chloride (Cl⁻), fluoride (F⁻), and sulfate (SO₄²⁻) anions, as shown in Fig. 13b. It was observed that the anions followed an irregular pattern where the chloride and sulfate ions acted as enhancers. In contrast, the fluoride ion acted as an inhibitor. Due to fluoride ions' ability to interact with •OH radicals and positive h⁺ in the valence bands, as shown in the following equations (Eqs. 26–29), only 78.91 ± 1.48% of para-nitrophenol was decomposed in their presence⁹⁹.



Although the abovementioned reactions produced fluoride radicals, they are well-thought-out to be less reactive and more selective than the other anionic radicals. Moreover, the chloride and sulfate anions enhanced the photocatalytic performance. So, to comprehend this more clearly, it is vital to investigate the influence of each ion distinctly. The salinity test revealed that chloride ion (Cl⁻) marginally accelerates para-nitrophenol breakdown (Fig. 13c). Moreover, chloride ions can interact with hydroxide and positive hole radicals to produce chloride and

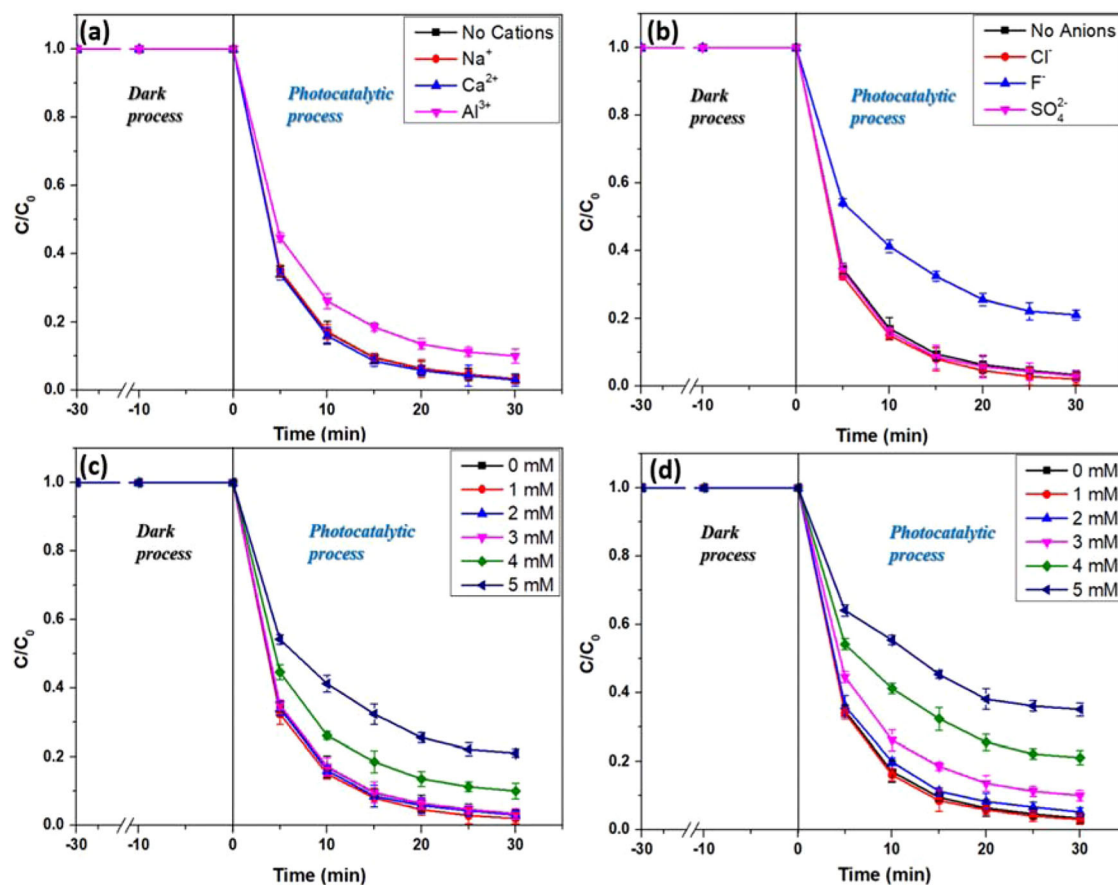


Fig. 13 Influence of co-existing species on para-nitrophenol removal by Cd/CdIn₂S₄@Ch quantum dots. Effect of (a) cations, (b) anions, (c) salinity, (d) sulfate ions on the photodegradation of para-nitrophenol; Reaction conditions: PNP concentration—15 ppm; catalyst dosage—12 mg; pH—3; H₂O₂ dosage—0.3 mL. Error bars represent the standard deviations.

chlorine radicals. The generated ROSs and the created radicals ($\bullet\text{Cl}$ and $\text{Cl}_2^{\bullet-}$) contribute to the breakdown of para-nitrophenol. It can be inferred that the para-nitrophenol degradation was boosted in the presence of salt at concentrations of 1 mM and 2 mM, with a removal efficiency of $98.01 \pm 1.31\%$ and $97.11 \pm 1.11\%$, respectively. Then, the efficiency stayed almost constant with the standard solution at a salt concentration of 3 mM with a photodegradation efficiency of $96.66 \pm 1.46\%$. However, the removal efficacy reduced at salt concentrations of 4 mM and 5 mM to $90.05 \pm 2.31\%$ and $78.95 \pm 1.2\%$, respectively. Compared to hydroxide radicals, chloride ions have a stronger affinity for positive holes, which can stop the reassembly of electrons and holes. Moreover, chloride ions may function as hydroxide scavengers, forming chloride and chlorine radicals, as illustrated below when interacting with hydroxide radicals (Eqs. 30–34)¹⁰⁰.

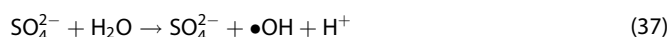
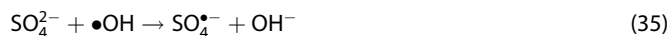


Despite having less oxidation potential than $\bullet\text{OH}$, the resulting anion radical species ($\bullet\text{Cl}$, $\text{Cl}_2^{\bullet-}$) are nonetheless regarded as reactive species toward organic molecules and can thus contribute to the breakdown of phenols. Thus, it can be concluded that for the efficient photodegradation of organic compounds like

para-nitrophenol, radical anions are more effective compared to $\bullet\text{OH}$ radicals due to their slower deactivation and recombination rate¹⁰¹. On the other hand, if they are not interacting with anions, the hydroxide radicals can be inactivated. As a result, even if anionic radicals are less reactive than $\bullet\text{OH}$, their greater availability will improve the entire photocatalytic process. In other words, $\bullet\text{OH}$ radicals are protected from ineffective deactivation by chloride ions by converting them into chloride and chlorine radicals. When chloride ions are present in very high concentrations, more Cl^- is present than is required for a reaction with hydroxide radicals ($\bullet\text{OH}$). Chloride ions may, therefore, gather on the surface of the synthesized photocatalyst and subsequently function as inhibitors rather than enhancers. Both the adsorption of the catalyst and the light absorption may be impacted by the presence of chloride ions in very high concentrations. Our analysis shows chloride ions may compete for adsorption sites on the Cd/CdIn₂S₄@Ch active surface at high concentrations. As a result, the amount of para-nitrophenol that can be adsorbed may be reduced. The degradation rate thus slows down. Hence, it was concluded that para-nitrophenol photodegradation was not affected adversely even at high salinity, as the variation in water salinity had little impact on the performance of synthesized Cd/CdIn₂S₄@Ch quantum dots.

Moreover, the presence of 1 mM sulfate ion improved the degradation performance with a removal efficiency of $97.01 \pm 1.42\%$. However, as the concentration of sulfate ion (SO_4^{2-}) rises, the elimination ability declines with a degradation efficiency of $94.87 \pm 1.31\%$, $90.04 \pm 1.49\%$, $79.08 \pm 2.13\%$, and $64.87 \pm 1.89\%$, in a concentration of 2 mM, 3 mM, 4 mM, and 5 mM, respectively, as shown in Fig. 13d. The decrease in the

efficiency at higher concentrations was accredited to the excess ions adsorbed on the nanocomposite surface, which hindered the para-nitrophenols from bonding to the active sites and decreased the overall light penetration proportion. According to Eqs. 35–37 sulfate ions behave similarly to chloride ions because they can interact with $\cdot\text{OH}$ radicals and positive holes in the valence band to form sulfate radicals. The generated radical showed very high oxidizing ability and could participate in the breakdown of para-nitrophenol along with reactive oxygen species, leading to a higher removal rate than in the standard solution ($96.70 \pm 1.31\%$, no ions)¹⁰². In addition, the sulfate anion reacted with water molecules to produce more $\cdot\text{OH}$ radicals and even prevent the recombination of electrons and holes, thus increasing the overall degradation performance¹⁰³.



Effect of water types

The influence of three different water matrices on the catalytic photodegradation of ofloxacin and para-nitrophenol was evaluated, as revealed in Supplementary Fig. 7a, b, respectively. It was found that these environmental waters possessed an inhibiting effect, reducing the degradation efficiency of synthesized Cd/CdIn₂S₄@Ch quantum dots. Compared to pure water, the photocatalyst showed decreased efficiency for ofloxacin and para-nitrophenol, with an efficiency of $78.96 \pm 1.47\%$ and $81.43 \pm 2.4\%$ for mineral water, $72.00 \pm 2.14\%$ and $80.12 \pm 1.98\%$ for tap water, and $60.22 \pm 2.24\%$ and $72.44 \pm 1.31\%$ for lake water, respectively. The general decrease in the photocatalyst's ability to degrade in these environmental waters can be accredited to several factors, the most important of which are light attenuation and the existence of different photocatalysis-inhibiting inorganic ions and organic substances in varying concentrations in the aforementioned water matrices¹⁰⁴. The higher mineral content of lake water compared to tap water may be the reason for the photocatalyst's poorer performance in the former matrix.

In summary, the goal of the current study was to investigate the photocatalytic performance of prepared Cd/CdIn₂S₄@Ch quantum dots, where CdIn₂S₄ was encapsulated in a chitosan matrix, as well as the influence of different reaction parameters, organic and inorganic compounds, and water matrices on the performance in the photodegradation of contaminants like ofloxacin and para-nitrophenol. The self-assembly of the ternary chalcogenide on chitosan biopolymer led to lattice strain, which decreased lattice parameters and increased distortion, leading to cadmium doping in the vacant interstitial sites. This self-doped cadmium led to enhanced surface charge transfer and slowed the recombination rate. The photocatalytic efficiency of the quantum dots was improved by H₂O₂. The AOP-mediated degradation showed excellent photocatalytic activity for ofloxacin and para-nitrophenol with an efficiency of $85.51 \pm 1.35\%$ and $96.70 \pm 1.31\%$, respectively, with a rate constant of 0.02334 and 0.15134 min^{-1} , in optimized condition. The scavenger test also concluded that the $\cdot\text{OH}$ and $\cdot\text{O}_2^-$ radicals played a significant role in the degradation process. It was found that the total COD was reduced by $80.67 \pm 1.67\%$ and $88.36 \pm 1.43\%$ from their initial values of $720 \text{ mg O}_2 \text{ L}^{-1}$ and $135 \text{ mg O}_2 \text{ L}^{-1}$, respectively, for 20 ppm of ofloxacin and 15 ppm of para-nitrophenol. Furthermore, the degradation pathways and intermediates were also analyzed to understand the mechanism of the degradation process. Although considered hydroxyl radical quenchers, chloride, fluoride, and sulfate were found to have minimal photodegradation effects when different anions were examined. Al³⁺ ions, on the

other hand, among cations, produced a sizeable rapid decline in photocatalytic performance because of their high charge density and capacity to adsorb on the photocatalyst surface. The effect of organic compounds such as humic acid, water salinity, and various water types on the degradation process was also examined, and as a result, the photocatalytic efficiency decreased. Last but not least, the reusability tests revealed remarkable photostability, which was established by TEM, EDX, and XRD analysis, demonstrating that the produced Cd/CdIn₂S₄@Ch quantum dots could be regenerated and recyclable for up to six consecutive cycles with no substantial reduction in its photoactivity.

METHODS

Reagents

Chitosan, indium chloride tetrahydrate (InCl₃·4H₂O) (99.9%), cadmium chloride monohydrate (CdCl₂·H₂O) (99.9%), thiourea (CH₄N₂S) (97%), ethylene glycol (C₂H₆O₂) (98%), hydrochloric acid (HCl), ofloxacin (C₁₈H₂₀FN₃O₄), para-nitrophenol (C₆H₅NO₃), ethanol (C₂H₅OH) (99.9%), benzoic acid (C₇H₆O₂) (99.5%), benzoquinone (C₆H₄O₂) (98%), potassium persulfate (K₂S₂O₈) (95%), disodium EDTA (Na₂-EDTA), sodium sulfate (Na₂SO₄) (99%), calcium sulfate (CaSO₄) (99%), aluminum sulfate (Al₂(SO₄)₃) (99.9%), sodium chloride (NaCl) (99.5%), sodium fluoride (NaF) (99%), urea (CH₄N₂O) (99%), humic acid sodium salt (C₉H₈Na₂O₄), and sodium dodecyl sulfate (NaC₁₂H₂₅SO₄).

The aforementioned compounds were purchased from Sigma Aldrich. Since they were of analytical quality, additional purification was unnecessary before usage. Throughout this experiment, de-ionized water was utilized in several phases.

Even though photocatalytic degradation studies are focused on environmental applications, most experiments are carried out in pure water. There has not been much research on how actual water samples affect the catalytic breakdown of toxic contaminants. The impact of numerous individual organic compounds and inorganic ions, along with water salinity, were studied to understand how different components affect the photodegradation of contaminants. This was followed by examining the photocatalyst's performance in actual water models like mineral water bottles, tap, and river water, on toxic contaminants like ofloxacin and para-nitrophenol (Table 4). Moreover, the packaged mineral water, with a pH of 7.25, was bought at a nearby convenience store. Local water systems provided easy access to tap water with a pH of 7.88, while the lake at NIT Silchar in India's Assam state served as the model for the river water matrices with a pH of 8.16.

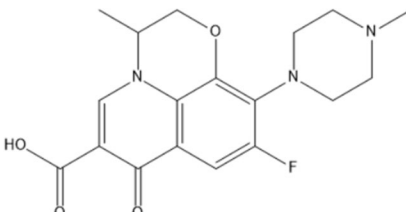
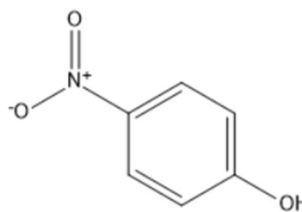
Synthesis of CdIn₂S₄

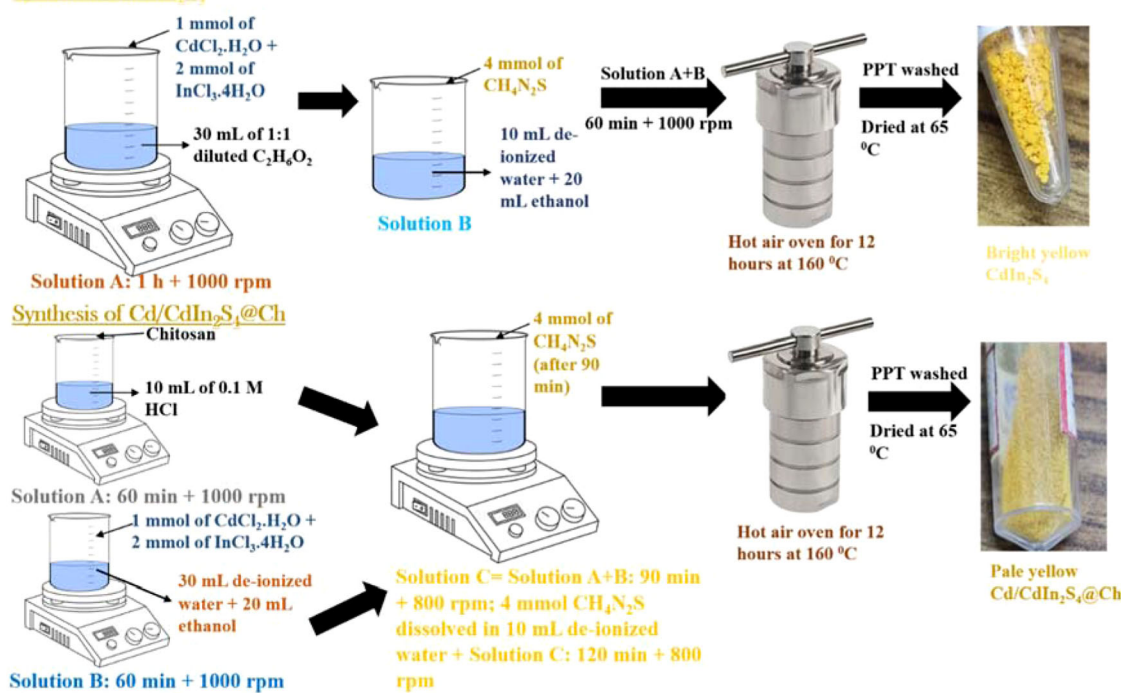
The pristine CdIn₂S₄ was fabricated by the facile solvothermal technique using thiourea as the sulfur source (Fig. 14). Solution A included 1 mmol of CdCl₂·H₂O (0.201 g) and 2 mmol of InCl₃·4H₂O (0.586 g), which were added to 30 mL of 1:1 diluted C₂H₆O₂ and agitated for 60 min at 1000 rpm. Solution B was prepared by adding 4 mmol of CH₄N₂S (0.304 g) into 10 mL of water and adding the solution to 20 mL of ethanol. The presence of ethanol in the solvothermal reaction would decrease the crystallization temperature¹⁰⁵. Further, Solution B was added to solution A slowly, forming solution C, with continuous stirring for up to 1 h. Solution C was transferred to the Teflon container, sealed in an autoclave, and kept in a hot air oven for 12 h at 160 °C. As a result, a bright yellow precipitate was obtained, washed with de-ionized water and ethanol, and dried at 65 °C until the final product was obtained.

Synthesis of Cd/CdIn₂S₄@Ch quantum dots

The Cd/CdIn₂S₄@Ch quantum dots were synthesized by developing pristine CdIn₂S₄ on the chitosan surface through the

Table 4. Properties of the model contaminants.

Properties	Ofloxacin	Para-nitrophenol
Molecular formula	$C_{18}H_{20}FN_3O_4$	$C_6H_5NO_3$
Molecular weight	361.373 g/mol	139.11 g/mol
Solubility	28.3 mg/mL	32.8 mg/mL
pK _a	8.31	7.15
Structure		

Synthesis of CdIn₂S₄**Fig. 14 Fabrication procedure.** Illustration depicting synthesis of pristine CdIn₂S₄ and Cd/CdIn₂S₄@Ch quantum dots.

solvothermal method (Fig. 14). Chitosan (0.5 g) was added to 10 mL of 0.1 M HCl solution and agitated for 1 h at 1000 rpm over moderate heat (Solution A). 2 mmol of InCl₃·4H₂O (0.586 g) and 1 mmol of CdCl₂·H₂O (0.201 g) were dissolved in 30 mL de-ionized water and 20 mL ethanol and agitated for 1 h at 1000 rpm (Solution B). Then, solution B was added to solution A, and the combined solution (Solution C) was heated and agitated for 1.5 h at 800 rpm. With continual stirring, 4 mmol of CH₄N₂S (0.304 g) was dissolved in 10 mL de-ionized water, and the solution was added to solution C. The final solution was maintained under magnetic stirring for 2 h, and the resulting solution was transferred to a Teflon container and sealed in an autoclave for 12 h at 160 °C. The obtained pale-yellow precipitate was centrifuged, washed with ethanol and de-ionized water, and dried at 65 °C until the desired product was obtained. The synthesis was surfactant-free and environmentally benign, as the chitosan acted as a template for the synthesis procedure. After

self-assembly of CdIn₂S₄ on the surface of HCl-treated chitosan biopolymer, the encapsulation resulted in the in-situ doping of Cadmium atoms in the interstitial sites of CdIn₂S₄ due to the competitive stress, which led to the rearrangement of the lattice structure resulting in the formation of Cd/CdIn₂S₄@Ch quantum dots.

Material characterization

The CdIn₂S₄ and Cd/CdIn₂S₄@Ch X-ray diffraction investigations were executed by a Philips X'PERT powder X-ray diffractometer with Cu K_α radiation. The Varian Cary eclipse fluorescence spectrophotometer was used to record photoluminescence spectra. The surface functional groups of pristine CdIn₂S₄ and Cd/CdIn₂S₄@Ch were evaluated using Fourier transform infrared spectroscopy (FT-IR, Niagoli IS50, USA) in the range of 500–4000 cm⁻¹. To investigate the morphology, size, and

diffraction rings of Cd/CdIn₂S₄@Ch, TEM, HRTEM, and SAED were performed using the JEOL JEM 2100 instrument. The FEI Quanta FEG 200-High Resolution Scanning Electron Microscope was used to perform SEM, EDX, and mapping in order to assess the framework, elemental makeup, and distribution of the elements. To further find out the thermal decomposition temperature of Cd/CdIn₂S₄@Ch, differential scanning calorimetry (DSC) and thermal thermogravimetric analyses (TGA) were executed by SDT Q600 of TA Instrument. X-ray photoelectron spectroscopy of Cd/CdIn₂S₄@Ch was accomplished using a PHI 5000 VersaProbe III spectrometer. Data for HRLCMS were obtained using the Xevo XS QToF mass spectrometer. Using a GENESYS 10S UV–visible spectrophotometer with a 1 cm quartz cell and a scan rate of 600 nm min⁻¹, the absorbance spectra of the liquid samples were recorded.

Photodegradation experiments

All photodegradation tests were carried out in 100 mL beakers with a working capacity of 50 mL, with a room-temperature irradiance of Philips 23 W white LED light source with 11,800 lx and radiation intensity of 52.73 W m⁻². A wooden chamber was used for the experimental setup, and an LED light source was mounted at the top. A beaker was positioned at the base of the chamber, 10 cm away from the bulb, and a magnetic stirrer was used to regulate the agitation speed during the photocatalytic reaction. All the tests were performed in the optimized conditions of 0.2 and 0.3 mL H₂O₂, pH of 7 and 3, catalyst dose of 10 mg and 12 mg, and contaminant concentration of 20 ppm and 15 ppm for ofloxacin, and para-nitrophenol respectively, and for other compounds as well at room temperature of 25 °C. Environmental water samples were also used as aqueous matrices in other experimental series. The solution mixture was kept in the dark with constant stirring for 30 min to achieve adsorption-desorption equilibrium before being exposed to LED irradiation for 90 min and 30 min, respectively, for the catalytic photodegradation of ofloxacin and para-nitrophenol. Adsorption of about 2–3% was observed for the pollutants; hence, it was considered negligible for all the conducted experiments. Each test for the assessment of photocatalysis was carried out in a quintet. Tracking the absorbance at the maximum wavelength of ofloxacin at 289 nm and para-nitrophenol at 400 nm at intervals of 10 and 5 min, respectively, allowed us to keep track of the photodegradation. The chemical oxygen demand (COD) was calculated using the conventional approach. For solutions containing H₂O₂, an additional 10% Na₂SO₃ solution was added, and the solution was heated under air to oxidize extra Na₂SO₃ in order to limit H₂O₂'s interference in the COD tests¹⁰⁶.

The following Eq. (38) was used to compute the photocatalytic degradation efficiency:

$$\text{Degradation Efficiency(\%)} = \left(\frac{C_0 - C}{C_0} \right) \times 100 \quad (38)$$

C₀ is the initial concentration, and C is the concentration at different time intervals for ofloxacin and para-nitrophenol. The kinetics of the photocatalytic process followed the following Eq. (39):

$$\ln\left(\frac{C_0}{C}\right) = kt \quad (39)$$

where *k* is the specific reaction rate constant of the pseudo-first-order reaction and C₀ and C are the corresponding concentrations at *t* = 0 and *t* = *t*.

The following equations, Eqs. (40) and (41), were used to calculate the photocatalytic systems' quantum yield and Figure of

Merit (FoM)¹⁰⁷.

$$\text{Quantum Yield} = \frac{\text{Decay rate} \left[\frac{\text{Molecules}}{\text{sec}} \right]}{\text{Photon Flux} \left[\frac{\text{Photons}}{\text{sec}} \right]} \quad (40)$$

$$\text{FoM} = \frac{\text{Conversion Efficiency(\%)}}{\text{Catalyst mass(mg)} \times \text{Initial concentration(ppm)} \times \text{Irradiation time(min)} \times \text{Applied power(W)}} \quad (41)$$

For five runs of the experiment under a specific set of circumstances, the error bars in the photodegradation plots exhibited slight standard deviations and were evidence of fair reproducibility.

DATA AVAILABILITY

All data generated or analyzed during this study are included in this published article (and its [supplementary information files](#)).

Received: 4 May 2023; Accepted: 2 November 2023;

Published online: 16 November 2023

REFERENCES

- Mishra, S. R. & Ahmaruzzaman, M. CuO and CuO-based nanocomposites: synthesis and applications in environment and energy. *Sustain. Mater. Technol.* **33**, e00463 (2022).
- Taghavi, R. et al. Magnetite metal–organic frameworks: applications in environmental remediation of heavy metals, organic contaminants, and other pollutants. *Inorg. Chem.* **61**, 15747–15783 (2022).
- Mishra, S. R. & Ahmaruzzaman, M. Tin oxide based nanostructured materials: synthesis and potential applications. *Nanoscale* **14**, 1566–1605 (2022).
- Hapeshi, E. et al. Drugs degrading photocatalytically: kinetics and mechanisms of ofloxacin and atenolol removal on titania suspensions. *Water Res.* **44**, 1737–1746 (2010).
- Xu, J. et al. Occurrence of antibiotics and antibiotic resistance genes in a sewage treatment plant and its effluent-receiving river. *Chemosphere* **119**, 1379–1385 (2015).
- Mohanta, D., Mahanta, A., Mishra, S. R., Jasimuddin, S. & Ahmaruzzaman, M. Novel SnO₂@ZIF-8/gC₃N₄ nanohybrids for excellent electrochemical performance towards sensing of p-nitrophenol. *Environ. Res.* **197**, 111077 (2021).
- Yadav, G. & Ahmaruzzaman, M. New generation advanced nanomaterials for photocatalytic abatement of phenolic compounds. *Chemosphere* **304**, 135297 (2022).
- Karimi-Maleh, H. et al. State-of-art advances on removal, degradation and electrochemical monitoring of 4-aminophenol pollutants in real samples: a review. *Environ. Res.* **222**, 115338 (2023).
- Tokazhanov, G., Han, S. & Lee, W. Enhanced catalytic reduction of p-nitrophenol by nano zerovalent iron - supported metal catalysts. *Catal. Commun.* **158**, 106337 (2021).
- Asgari, E. et al. Heterogeneous catalytic degradation of nonylphenol using persulphate activated by natural pyrite: response surface methodology modelling and optimisation. *Int. J. Environ. Anal. Chem.* **2022**, 6041–6060 (2020).
- Mishra, S. R. & Ahmaruzzaman, M. Cerium oxide and its nanocomposites: structure, synthesis, and wastewater treatment applications. *Mater. Today Commun.* **28**, 102562 (2021).
- Bhuyan, A. & Ahmaruzzaman, M. Novel Zn(II)-imidazolate polymorph MOF loaded with Mo-QD clusters for solar light-driven H₂O₂-assisted synergistic photosensitized degradation of gentian violet. *J. Alloys Compd.* **950**, 169747 (2023).
- Zhang, X. W. et al. Immobilized N-C/Co derived from ZIF-67 as PS-AOP catalyst for effective tetracycline matrix elimination: From batch to continuous process. *Chem. Eng. J.* **450**, 138082 (2022).
- Wu, X. et al. Engineering controllable oxygen vacancy defects in iron hydroxide oxide immobilized on reduced graphene oxide for boosting visible light-driven photo-Fenton-like oxidation. *J. Colloid Interface Sci.* **623**, 9–20 (2022).
- Bhuyan, A. & Ahmaruzzaman, M. Metal-organic frameworks: a new generation potential material for aqueous environmental remediation. *Inorg. Chem. Commun.* **140**, 109436 (2022).
- Arefi-Oskoui, S. et al. Development of MoS₂/O-MWCNTs/PES blended membrane for efficient removal of dyes, antibiotic, and protein. *Sep. Purif. Technol.* **280**, 119822 (2022).

17. Begum, S., Ranjan Mishra, S. & Ahmaruzzaman, M. Facile synthesis of NiO-SnO₂ nanocomposite for enhanced photocatalytic degradation of bismarck brown. *Inorg. Chem. Commun.* **143**, 109721 (2022).
18. Mohammadi, R. et al. Visible-light-driven photocatalytic activity of ZnO/g-C₃N₄ heterojunction for the green synthesis of biologically interest small molecules of thiazolidinones. *J. Photochem. Photobiol. A: Chem.* **402**, 112786 (2020).
19. Yadav, G. & Ahmaruzzaman, M. ZnIn₂S₄ and ZnIn₂S₄ based advanced hybrid materials: structure, morphology and applications in environment and energy. *Inorg. Chem. Commun.* **138**, 109288 (2022).
20. Zhang, Y. J., Tang, H. M. & Gao, S. P. Density functional theory study of ZnIn₂S₄ and CdIn₂S₄ polymorphs using full-potential linearized augmented plane wave method and modified Becke–Johnson potential. *Phys. Status Solidi* **257**, 1900485 (2020).
21. He, J. et al. Ultra-thin CdIn₂S₄ nanosheets with nanoholes for efficient photocatalytic hydrogen evolution. *Opt. Mater. (Amst.)* **108**, 112031 (2020).
22. Ling, C. et al. Solvothermal synthesis of CdIn₂S₄ photocatalyst for selective photosynthesis of organic aromatic compounds under visible light. *Sci. Rep.* **7**, 1–16 (2017).
23. Yu, X.-D., Xue-Song, Q., Yi-Hang, G. & C.-W, H. Photocatalytic dye methyl orange decomposition on ternary sulfide (CdIn₂S₄) under visible-light. *Chinese Chem. Lett.* **16**, 1259–1262 (2005).
24. Bariki, R., Majhi, D., Das, K., Behera, A. & Mishra, B. G. Facile synthesis and photocatalytic efficacy of UiO-66/CdIn₂S₄ nanocomposites with flowerlike 3D-microspheres towards aqueous phase decontamination of triclosan and H₂ evolution. *Appl. Catal. B: Environ.* **270**, 118882 (2020).
25. Li, Y., Wang, X., Xia, Y. & Gao, L. A novel visible-light-driven photo-fenton system composed of Fe-doped CdIn₂S₄/g-C₃N₄ heterojunction and H₂O₂ to remove methyl orange. *Ind. Eng. Chem. Res.* https://doi.org/10.1021/ACS.IECR.2C00276/ASSET/IMAGES/MEDIUM/IE2C00276_M022.GIF (2022).
26. de Lima, P. H. C. et al. Recent advances on nanohybrid systems constituting clay–chitosan with organic molecules—a review. *Appl. Clay Sci.* **226**, 106548 (2022).
27. Yu, J. et al. Current trends and challenges in the synthesis and applications of chitosan-based nanocomposites for plants: a review. *Carbohydr. Polym.* **261**, 117904 (2021).
28. Kale, B. B. et al. CdIn₂S₄ nanotubes and “marigold” nanostructures: a visible-light photocatalyst. *Adv. Funct. Mater.* **16**, 1349–1354 (2006).
29. Cao, Z. et al. Enhancing luminescence of intrinsic and Mn doped CsPbCl₃ perovskite nanocrystals through Co²⁺ doping. *Mater. Res. Bull.* **121**, 110608 (2020).
30. Jiang, A. Q., Li, G. H. & Zhang, L. D. Dielectric study in nanocrystalline Bi₄Ti₃O₁₂ prepared by chemical coprecipitation. *J. Appl. Phys.* **83**, 4878 (1998).
31. Tang, E. S. K., Huang, M. & Lim, L. Y. Ultrasonication of chitosan and chitosan nanoparticles. *Int. J. Pharm.* **265**, 103–114 (2003).
32. Schmidt, W. Calculation of XRD patterns of simulated FDU-15, CMK-5, and CMK-3 carbon structures. *Microporous Mesoporous Mater.* **117**, 372–379 (2009).
33. Ganesh, I. A review on magnesium aluminate (MgAl₂O₄) spinel: synthesis, processing and applications. *Int. Mater. Rev.* **58**, 63–112 (2013).
34. Li, Y., Dillert, R. & Bahnemann, D. Preparation of porous CdIn₂S₄ photocatalyst films by hydrothermal crystal growth at solid/liquid/gas interfaces. *Thin Solid Films* **516**, 4988–4992 (2008).
35. Xue, C. et al. Spatial charge separation and transfer in ultrathin CdIn₂S₄/rGO nanosheet arrays decorated by ZnS quantum dots for efficient visible-light-driven hydrogen evolution. *Nano Energy* **39**, 513–523 (2017).
36. Zhang, J. et al. Ternary NiS/Zn_xCd_{1-x}S/reduced graphene oxide nanocomposites for enhanced solar photocatalytic H₂-production activity. *Adv. Energy Mater.* **4**, 1301925 (2014).
37. Zheng, B., Luo, Y., Liao, H. & Zhang, C. Investigation of the crystallinity of suspension plasma sprayed hydroxyapatite coatings. *J. Eur. Ceram. Soc.* **37**, 5017–5021 (2017).
38. Gadore, V., Mishra, S. R. & Ahmaruzzaman, M. Green and environmentally sustainable fabrication of SnS₂ quantum dots/chitosan nanocomposite for enhanced photocatalytic performance: effect of process variables, and water matrices. *J. Hazard. Mater.* **444**, 130301 (2023).
39. Pathania, D. et al. Photocatalytic degradation of highly toxic dyes using chitosan-g-poly(acrylamide)/ZnS in presence of solar irradiation. *J. Photochem. Photobiol. A: Chem.* **329**, 61–68 (2016).
40. Sirajudheen, P., Kasim, V. C. R., Nabeena, C. P., Basheer, M. C. & Meenakshi, S. Tunable photocatalytic oxidation response of ZnS tethered chitosan-polyaniline composite for the removal of organic pollutants: a mechanistic perspective. *Mater. Today Proc.* **47**, 2553–2559 (2021).
41. Nafees, M., Liaqut, W., Ali, S. & Shafique, M. A. Synthesis of ZnO/Al:ZnO nanomaterial: structural and band gap variation in ZnO nanomaterial by Al doping. *Appl. Nanosci.* **3**, 49–55 (2013).
42. Ng, J. C. Y., Cheung, W. H. & McKay, G. Equilibrium studies of the sorption of Cu(II) ions onto chitosan. *J. Colloid Interface Sci.* **255**, 64–74 (2002).
43. Liu, B. et al. Efficient charge separation between UiO-66 and ZnIn₂S₄ flowerlike 3D microspheres for photoelectronchemical properties. *Appl. Catal. B: Environ.* **226**, 234–241 (2018).
44. Li, C. et al. Photocatalysis over NH₂-UiO-66/CoFe₂O₄/CdIn₂S₄ double p-n junction: significantly promoting photocatalytic performance by double internal electric fields. *Chem. Eng. J.* **435**, 134740 (2022).
45. Wang, Q. et al. Photochemical preparation of Cd/CdS photocatalysts and their efficient photocatalytic hydrogen production under visible light irradiation. *Green Chem.* **16**, 2728–2735 (2014).
46. Cai, Y. et al. Easy incorporation of single-walled carbon nanotubes into two-dimensional MoS₂ for high-performance hydrogen evolution. *Nanotechnology* **25**, 465401 (2014).
47. Daniyal, W. M. E. M. M. et al. X-ray photoelectron spectroscopy analysis of chitosan–graphene oxide-based composite thin films for potential optical sensing applications. *Polymers (Basel)* **13**, 478 (2021).
48. Yuan, D., Cadien, K., Liu, Q. & Zeng, H. Adsorption characteristics and mechanisms of O-Carboxymethyl chitosan on chalcopyrite and molybdenite. *J. Colloid Interface Sci.* **552**, 659–670 (2019).
49. Gieroba, B. et al. Spectroscopic studies on the temperature-dependent molecular arrangements in hybrid chitosan/1,3-β-D-glucan polymeric matrices. *Int. J. Biol. Macromol.* **159**, 911–921 (2020).
50. Queiroz, M. F., Melo, K. R. T., Sabry, D. A., Sasaki, G. L. & Rocha, H. A. O. Does the use of chitosan contribute to oxalate kidney stone formation? *Mar. Drugs* **13**, 141–158 (2014).
51. Melo-Silveira, R. F. et al. In vitro antioxidant, anticoagulant and antimicrobial activity and in inhibition of cancer cell proliferation by xylan extracted from corn cobs. *Int. J. Mol. Sci.* **13**, 409–426 (2011).
52. Lim, S. H. & Hudson, S. M. Synthesis and antimicrobial activity of a water-soluble chitosan derivative with a fiber-reactive group. *Carbohydr. Res.* **339**, 313–319 (2004).
53. Tantalaja, J., Thumanu, K. & Rachtanapun, C. An assessment of antibacterial mode of action of chitosan on *Listeria innocua* cells using real-time HATR-FTIR spectroscopy. *Int. J. Biol. Macromol.* **135**, 386–393 (2019).
54. Palas, B., Ersöz, G. & Atalay, S. Photo Fenton-like oxidation of tartrazine under visible and UV light irradiation in the presence of LaCuO₃ perovskite catalyst. *Process Saf. Environ. Prot.* **111**, 270–282 (2017).
55. Raha, S. & Ahmaruzzaman, M. Enhanced performance of a novel super-paramagnetic g-C₃N₄/NiO/ZnO/Fe₃O₄ nanohybrid photocatalyst for removal of esomeprazole: Effects of reaction parameters, co-existing substances and water matrices. *Chem. Eng. J.* **395**, 124969 (2020).
56. Ahmaruzzaman, M. & Mishra, S. R. Photocatalytic performance of g-C₃N₄ based nanocomposites for effective degradation/removal of dyes from water and wastewater. *Mater. Res. Bull.* **143**, 111417 (2021).
57. Begum, S., Mishra, S. R. & Ahmaruzzaman, M. Fabrication of ZnO-SnO₂ nanocomposite and its photocatalytic activity for enhanced degradation of Biebrich scarlet. *Environ. Sci. Pollut. Res.* **2022** 1–14 <https://doi.org/10.1007/S11356-022-21851-1> (2022).
58. Dai, C. et al. Surface facet of CuFeO₂ nanocatalyst: a key parameter for H₂O₂ activation in Fenton-like reaction and organic pollutant degradation. *Environ. Sci. Technol.* **52**, 6518–6525 (2018).
59. Bhatia, V., Ray, A. K. & Dhir, A. Enhanced photocatalytic degradation of ofloxacin by co-doped titanium dioxide under solar irradiation. *Sep. Purif. Technol.* **161**, 1–7 (2016).
60. Konstantinou, I. K. & Albanis, T. A. TiO₂-assisted photocatalytic degradation of azo dyes in aqueous solution: kinetic and mechanistic investigations: A review. *Appl. Catal. B: Environ.* **49**, 1–14 (2004).
61. Zhou, L. et al. Electro-Fenton degradation of p-nitrophenol using the anodized graphite felts. *Chem. Eng. J.* **233**, 185–192 (2013).
62. Gadore, V., Mishra, S. R. & Ahmaruzzaman, M. Bio-inspired sustainable synthesis of novel SnS₂/biochar nanocomposite for adsorption coupled photodegradation of amoxicillin and congo red: Effects of reaction parameters, and water matrices. *J. Environ. Manage.* **334**, 117496 (2023).
63. Georgaki, I., Vasilaki, E. & Katsarakis, N. A study on the degradation of carbamazepine and ibuprofen by TiO₂ & ZnO photocatalysis upon uv/visible-light irradiation. *Am. J. Anal. Chem.* **05**, 518–534 (2014).
64. Dey, A. K., Mishra, S. R. & Ahmaruzzaman, M. Solar light-based advanced oxidation processes for degradation of methylene blue dye using novel Zn-modified CeO₂/biochar. *Environ. Sci. Pollut. Res.* **30**, 53887–53903 (2023).
65. Ma, S. et al. Maximally exploiting active sites on Yolk@shell nanoreactor: Nearly 100% PMS activation efficiency and outstanding performance over full pH range in Fenton-like reaction. *Appl. Catal. B Environ.* **316**, 121594 (2022).
66. Abellán, M. N., Bayarri, B., Giménez, J. & Costa, J. Photocatalytic degradation of sulfamethoxazole in aqueous suspension of TiO₂. *Appl. Catal. B: Environ.* **74**, 233–241 (2007).

67. Barakat, N. A. M., Kanjwal, M. A., Chronakis, I. S. & Kim, H. Y. Influence of temperature on the photodegradation process using Ag-doped TiO₂ nanostructures: negative impact with the nanofibers. *J. Mol. Catal. A: Chem.* **366**, 333–340 (2013).
68. Prasetyoko, D. et al. Mesoporous ZnO nanoparticles using gelatin—Pluronic F127 as a double colloidal system for methylene blue photodegradation. *Korean J. Chem. Eng.* **40**, 112–123 (2023).
69. Zhao, H., Xia, Q., Xing, H., Chen, D. & Wang, H. Construction of pillared-layer MOF as efficient visible-light photocatalysts for aqueous Cr(VI) reduction and dye degradation. *ACS Sustain. Chem. Eng.* **5**, 4449–4456 (2017).
70. Maurino, V. et al. The fate of organic nitrogen under photocatalytic conditions: degradation of nitrophenols and aminophenols on irradiated TiO₂. *J. Photochem. Photobiol. A: Chem.* **109**, 171–176 (1997).
71. Vikrant, K., Park, C. M., Kim, K. H., Kumar, S. & Jeon, E. C. Recent advancements in photocatalyst-based platforms for the destruction of gaseous benzene: Performance evaluation of different modes of photocatalytic operations and against adsorption techniques. *J. Photochem. Photobiol. C: Photochem. Rev.* **41**, 100316 (2019).
72. Ebrahimi, A. et al. A novel ternary heterogeneous TiO₂/BiVO₄/NaY-Zeolite nanocomposite for photocatalytic degradation of microcystin-leucine arginine (MC-LR) under visible light. *Ecotoxicol. Environ. Saf.* **210**, 111862 (2021).
73. Mansouri, A., Makris, D. P. & Kefalas, P. Determination of hydrogen peroxide scavenging activity of cinnamic and benzoic acids employing a highly sensitive peroxyoxalate chemiluminescence-based assay: Structure–activity relationships. *J. Pharm. Biomed. Anal.* **39**, 22–26 (2005).
74. Chen, X. et al. Synergy effect between adsorption and heterogeneous photo-Fenton-like catalysis on LaFeO₃/lignin-biochar composites for high efficiency degradation of ofloxacin under visible light. *Sep. Purif. Technol.* **280**, 119751 (2022).
75. Liu, Q. et al. Magnetic ZnO@Fe₃O₄ composite for self-generated H₂O₂ toward photo-Fenton-like oxidation of nitrophenol. *Compos. B: Eng.* **200**, 108345 (2020).
76. Ghoderao, K. P., Jamble, S. N. & Kale, R. B. Hydrothermally synthesized Cd-doped ZnO nanostructures with efficient sunlight-driven photocatalytic and antibacterial activity. *J. Mater. Sci. Mater. Electron.* **30**, 11208–11219 (2019).
77. Brou, Y. S. et al. Biopolymer effect on copper corrosion in 3.5 wt.% NaCl solution: electrochemical and quantum chemical studies. *Int. J. Corros. Scale Inhib.* **9**, 182–200 (2020).
78. Zhang, Q. et al. Self-assembly of CdS/CdIn₂S₄ heterostructure with enhanced photocascade synthesis of schiff base compounds in an aromatic alcohols and nitrobenzene system with visible light. *ACS Appl. Mater. Interfaces* **11**, 46735–46745 (2019).
79. Balyan, M., Nasution, T. I., Nainggolan, I., Mohamad, H. & Ahmad, Z. A. Effect band gap of chitosan film in converting water vapour into electrical current. *Mater. Sci. Forum* **1010**, 445–452 (2020).
80. Li, Y., Wang, X., Xia, Y. & Gao, L. A novel visible-light-driven photo-fenton system composed of Fe-doped CdIn₂S₄/g-C₃N₄ heterojunction and H₂O₂ to remove methyl orange. *Ind. Eng. Chem. Res.* **61**, 12905–12917 (2022).
81. Wang, W. et al. Photocatalytic hydrogen evolution and bacterial inactivation utilizing sonochemical-synthesized g-C₃N₄/red phosphorus hybrid nanosheets as a wide-spectral-responsive photocatalyst: the role of type I band alignment. *Appl. Catal. B: Environ.* **238**, 126–135 (2018).
82. Peng, Y. et al. A new strategy to construct cellulose-chitosan films supporting Ag/Ag₂O/ZnO heterostructures for high photocatalytic and antibacterial performance. *J. Colloid Interface Sci* **609**, 188–199 (2022).
83. Neena, D. et al. Enhanced visible light photodegradation activity of RhB/MB from aqueous solution using nanosized novel Fe-Cd co-modified ZnO. *Sci. Rep.* **8**, 1–12 (2018).
84. Zhang, D. & Zeng, F. Visible light-activated cadmium-doped ZnO nanostructured photocatalyst for the treatment of methylene blue dye. *J. Mater. Sci.* **47**, 2155–2161 (2012).
85. Zhang, M., Xu, J. & Chen, M. Novel Z-scheme LaVO₄/Bi₂O₃Cl₂ heterojunctions for highly efficient degradation of ofloxacin under visible light irradiation. *J. Alloys Compd.* **925**, 166653 (2022).
86. Azizi, S., Alidadi, H., Maaza, M. & Sarkhosh, M. Degradation of ofloxacin using the UV/ZnO/iodide process in an integrated photocatalytic-biological reactor containing baffles. *Ind. Eng. Chem. Res.* **59**, 22440–22450 (2020).
87. Huang, Z. et al. Facile fabrication of electrospun g-C₃N₄/Bi₂O₃/Cl₂/poly(acrylonitrile-co-maleic acid) heterojunction nanofibers for boosting visible-light catalytic ofloxacin degradation. *New J. Chem.* **46**, 3727–3737 (2022).
88. Patidar, R. & Srivastava, V. C. Mechanistic and kinetic insights of synergistic mineralization of ofloxacin using a sono-photo hybrid process. *Chem. Eng. J.* **403**, 125736 (2021).
89. Labhane, P. K., Sonawane, G. H. & Sonawane, S. H. Influence of rare-earth metal on the zinc oxide nanostructures: application in the photocatalytic degradation of methylene blue and p-nitro phenol. *Green Process. Synth.* **7**, 360–371 (2018).
90. Shaoqing, Y., Jun, H. & Jianlong, W. Radiation-induced catalytic degradation of p-nitrophenol (PNP) in the presence of TiO₂ nanoparticles. *Radiat. Phys. Chem.* **79**, 1039–1046 (2010).
91. Wang, C., Zhu, L., Wei, M., Chen, P. & Shan, G. Photolytic reaction mechanism and impacts of coexisting substances on photodegradation of bisphenol A by Bi₂WO₆ in water. *Water Res.* **46**, 845–853 (2012).
92. Quivet, E., Faure, R., Georges, J., Paissé, J. O. & Lantéri, P. Influence of metal salts on the photodegradation of imazapyr, an imidazolinone pesticide. *Pest Manag. Sci.* **62**, 407–413 (2006).
93. Hu, C., Yu, J. C., Hao, Z. & Wong, P. K. Effects of acidity and inorganic ions on the photocatalytic degradation of different azo dyes. *Appl. Catal. B: Environ.* **46**, 35–47 (2003).
94. Chen, Y., Yang, S., Wang, K. & Lou, L. Role of primary active species and TiO₂ surface characteristic in UV-illuminated photodegradation of Acid Orange 7. *J. Photochem. Photobiol. A: Chem.* **172**, 47–54 (2005).
95. García-Domínguez, Á. E. et al. Urea assisted synthesis of TiO₂-CeO₂ composites for photocatalytic acetaminophen degradation via simplex-centroid mixture design. *Results Eng* **14**, 100443 (2022).
96. Haroune, L., Salaun, M., Ménard, A., Legault, C. Y. & Bellenger, J. P. Photocatalytic degradation of carbamazepine and three derivatives using TiO₂ and ZnO: Effect of pH, ionic strength, and natural organic matter. *Sci. Total Environ.* **475**, 16–22 (2014).
97. Zhuang, R. & Wang, J. Degradation of diclofenac in aqueous solution by ionizing radiation in the presence of humic acid. *Sep. Purif. Technol.* **234**, 116079 (2020).
98. Rodríguez-López, L. et al. Influence of pH, humic acids, and salts on the dispersion of amoxicillin and azithromycin under simulated sunlight. *Spanish J. Soil Sci* **12**, 3 (2022).
99. Parrino, F., Livraghi, S., Giamello, E., Ceccato, R. & Palmisano, L. Role of hydroxyl, superoxide, and nitrate radicals on the fate of bromide ions in photocatalytic TiO₂ Suspensions. *ACS Catal* **10**, 7922–7931 (2020).
100. Al-Hasani, H., Al-Sabahi, J., Al-Ghafri, B., Al-Hajri, R. & Al-Abri, M. Effect of water quality in photocatalytic degradation of phenol using zinc oxide nanorods under visible light irradiation. *J. Water Process Eng* **49**, 103121 (2022).
101. Jyothi, K. P., Yesodharan, S. & Yesodharan, E. P. Contaminant salts as enhancers of sonocatalytic degradation of organic water pollutants: Effect of concentration, reaction time and adsorption on the efficiency of enhancement and the fate of concurrently formed H₂O₂. *J. Environ. Chem. Eng.* **6**, 3574–3589 (2018).
102. Bendjabeur, S., Zouaghi, R., Kaabeche, O. N. H. & Sehili, T. Parameters affecting adsorption and photocatalytic degradation behavior of gentian violet under UV irradiation with several kinds of TiO₂ as a photocatalyst. *Int. J. Chem. React. Eng.* **15** (2017).
103. Devi, L. G., Munikrishnapa, C., Nagaraj, B. & Rajashekhar, K. E. Effect of chloride and sulfate ions on the advanced photo Fenton and modified photo Fenton degradation process of Alizarin Red S. *J. Mol. Catal. A Chem.* **374–375**, 125–131 (2013).
104. Ganiyu, S. O., Sable, S. & Gamal El-Din, M. Advanced oxidation processes for the degradation of dissolved organics in produced water: a review of process performance, degradation kinetics and pathway. *Chem. Eng. J.* **429**, 132492 (2022).
105. Li, X., Odoom-Wubah, T., Chen, Z., Zheng, B. & Huang, J. Ethanol-dependent solvothermal synthesis of monodispersed YAG powders with precursor obtained through bubbling ammonia. *Ceram. Int.* **40**, 16317–16321 (2014).
106. Wang, Y., Li, W. & Irini, A. A novel and quick method to avoid H₂O₂ interference on COD measurement in Fenton system by Na₂SO₃ reduction and O₂ oxidation. *Water Sci. Technol.* **68**, 1529–1535 (2013).
107. Hayati, P. et al. Photocatalytic activity of new nanostructures of an Ag (i) metal-organic framework (Ag-MOF) for the efficient degradation of MCPA and 2, 4-D herbicides under sunlight irradiation. *New J. Chem.* **45**, 3408–3417 (2021).
108. Kaur, A., Umar, A., Anderson, W. A. & Kansal, S. K. Facile synthesis of CdS/TiO₂ nanocomposite and their catalytic activity for ofloxacin degradation under visible illumination. *J. Photochem. Photobiol. A: Chem.* **360**, 34–43 (2018).
109. Fazli, A., Zakeri, F., Khataee, A. & Orooji, Y. A BaTiO₃/WS₂ composite for piezocatalytic persulfate activation and ofloxacin degradation. *Commun. Chem.* **5**, 1–14 (2022).
110. Li, X. et al. BiOBr with oxygen vacancies capture 0D black phosphorus quantum dots for high efficient photocatalytic ofloxacin degradation. *Appl. Surf. Sci.* **593**, 153422 (2022).
111. Heidari, S., Haghighi, M. & Shabani, M. Sunlight-activated BiOCl/BiOBr-Bi₂O₃ photocatalyst for the removal of pharmaceutical compounds. *J. Clean. Prod.* **259**, 120679 (2020).
112. Zhang, W., Liu, Y. & Li, C. Photocatalytic degradation of ofloxacin on Gd₂Ti₂O₇ supported on quartz spheres. *J. Phys. Chem. Solids* **118**, 144–149 (2018).

113. Yang, Y. et al. Bicarbonate-enhanced iron-based Prussian blue analogs catalyze the Fenton-like degradation of p-nitrophenol. *J. Colloid Interface Sci* **608**, 2884–2895 (2022).
114. Guo, H. et al. Theoretical and experimental insight into plasma-catalytic degradation of aqueous p-nitrophenol with graphene-ZnO nanoparticles. *Sep. Purif. Technol.* **295**, 121362 (2022).
115. Sun, S. P. & Lemley, A. T. p-Nitrophenol degradation by a heterogeneous Fenton-like reaction on nano-magnetite: process optimization, kinetics, and degradation pathways. *J. Mol. Catal. A Chem.* **349**, 71–79 (2011).

AUTHOR CONTRIBUTIONS

S.R.M.: Conceptualization, Investigation, Visualization, Data Curation, Methodology, Writing—original draft, Writing—review & editing. V.G.: Data Curation, Methodology. M.A.: Writing—review & editing, Supervision.

COMPETING INTERESTS

The authors declare no competing interests

ADDITIONAL INFORMATION

Supplementary information The online version contains supplementary material available at <https://doi.org/10.1038/s41545-023-00291-5>.

Correspondence and requests for materials should be addressed to Md. Ahmaruzzaman.

Reprints and permission information is available at <http://www.nature.com/reprints>

Publisher's note Springer Nature remains neutral with regard to jurisdictional claims in published maps and institutional affiliations.



Open Access This article is licensed under a Creative Commons Attribution 4.0 International License, which permits use, sharing, adaptation, distribution and reproduction in any medium or format, as long as you give appropriate credit to the original author(s) and the source, provide a link to the Creative Commons license, and indicate if changes were made. The images or other third party material in this article are included in the article's Creative Commons license, unless indicated otherwise in a credit line to the material. If material is not included in the article's Creative Commons license and your intended use is not permitted by statutory regulation or exceeds the permitted use, you will need to obtain permission directly from the copyright holder. To view a copy of this license, visit <http://creativecommons.org/licenses/by/4.0/>.

© The Author(s) 2023